Monthly Notices of the ROYAL ASTRONOMICAL SOCIETY

MNRAS **549,** 1–28 (2026)
Advance Access publication 2026 May 21

https://doi.org/10.1093/mnras/stag948

Finding the evolutionary link between ULIRGs and radio galaxies

Ayisha Fida [1], Sumana Nandi [2]★, Mousumi Das [3], K. Rubinur [4], S. Shanbhog [5], Preeti Kharb [6] and Barenya Dev [7]

[1]*Manipal Centre for Natural Sciences, Centre of Excellence, Manipal Academy of Higher Education, Manipal, Karnataka 576104, India*
[2]*Institute of Astronomy Space and Earth Sciences, P 177, CIT Road, Scheme 7M, Kolkata 700054, West Bengal, India*
[3]*Indian Institute of Astrophysics, Koramangala II Block, Bangalore 560034, India*
[4]*Institute of Theoretical Astrophysics, University of Oslo, PO Box 1029 Blindern, 0315 Oslo, Norway*
[5]*Scuola Normale Superiore di Pisa, Piazza dei Cavalieri 7, I-56126 Pisa, Italy*
[6]*National Centre for Radio Astrophysics (NCRA) – Tata Institute of Fundamental Research (TIFR), S. P. Pune University Campus, Ganeshkhind, Pune 411007, India*
[7]*Department of Astronomy, Astrophysics and Space Engineering, Indian Institute of Technology Indore, Khandwa Road, Simrol, Indore 453552, Madhya Pradesh, India*

Accepted 2026 May 14. Received 2026 May 14; in original form 2025 December 12

ABSTRACT

Ultraluminous infrared galaxies (ULIRGs) are the remnants of the major mergers of gas-rich galaxies. They are dusty systems and are extremely luminous in the infrared. Both starbursts and active galactic nucleus (AGN) activity supply power in these systems, but it is not clear how these two activities are related to the overall evolution of the merger remnant. Studies suggest that there may be an evolutionary link between ULIRGs and radio galaxies. Radio observations of ULIRGs are a useful tool for understanding this evolutionary path as well as studying the energy contributions from starbursts and AGN. We perform a systematic census of these signatures in 38 ULIRGs using upgraded Giant Metrewave Radio Telescope observations and archival radio data. In the sample, 30 sources have enough frequency coverage to obtain their radio spectrum. Of these, 17 sources show a turnover frequency between 63 and 509 MHz and a spectral age variation from 0.009 to 44 Myr. Also, eight sources have extended structures with projected linear sizes varying from 0.7 to 11 kpc. Our results indicate that the primary energy source in these systems is the AGN rather than star formation. The majority of the ULIRGs in our sample, particularly those in the post-merger stage, exhibit gigahertz-peaked spectrum or compact steep spectrum-like characteristics, suggesting that they are evolving into young radio galaxies. We note that six sources with high star formation activity show a low-frequency turnover and a smaller spectral age; we confirm these six sources host buried AGN. This study enables us to trace the evolutionary link between ULIRGs and radio galaxies.

Key words: galaxies: active – galaxies: evolution – galaxies: interactions – galaxies: star formation – radio continuum: galaxies.

1 INTRODUCTION

Ultraluminous infrared galaxies (ULIRGs) are gas-rich merger remnants that have high-infrared (IR) luminosities of $L_{\rm IR} > 10^{12}\,{\rm L}_{\odot}$. They are an important population to understand the galaxy formation and evolution processes. They are distributed in both the local and high-redshift universe ($z \gtrsim 1-2$; C. J. Lonsdale, D. Farrah & H. E. Smith 2006; A. Sajina et al. 2007). The abundance of dust at sub-kpc scales in ULIRGs has made it difficult to study the main power production mechanism by direct optical observations. However, X-ray, near-IR, and radio observations which can penetrate the dust, have demonstrated that a significant number of ULIRGs are powered by both starburst and active galactic nucleus (AGN) activity. It has also been shown that a large fraction of ULIRGs show signatures of interaction in their optical images, which confirms that they are the result of the merger of two gas-rich spiral galaxies (S. Veilleux et al. 2009). Initially, these merger events affect the star formation rates (P. Calderón-Castillo & R. Smith 2024). However, as the merger evolves, star formation is quenched and the ULIRGs transform into either unobscured quasars or elliptical galaxies (S. Yamada et al. 2023). Therefore, the study of local universe ULIRGs can connect galaxy mergers, triggered star formation, nuclear activity, and the formation of quasars or elliptical galaxies (V. U 2022).

The radio emission in ULIRGs is mainly due to relativistic synchrotron radiation and free–free emission. Radio observations are thus important for tracing star-forming activity as well as AGN activity in ULIRGs. The well-known correlation between radio and far-IR (FIR) luminosities can be explained by star formation and starburst activity (M. S. Yun et al. 2001), whereas the integrated synchrotron spectrum, detection of turnover, spectral age, identification of peak radio intensity, and brightness temperature estimation can verify the presence of AGN in ULIRGs. Several excellent works have described properties of star formation versus AGN power (S. Veilleux et al. 2009; V. U 2022), interactions and

★ E-mail: sumana1981@gmail.com

mergers (S. Veilleux et al. 2002), molecular outflows (C. Cicone et al. 2018), dust content in ULIRGs (J. A. Rich, L. J. Kewley & M. A. Dopita 2011). In some cases, the AGNs are hidden behind thick dust columns, and it is extremely difficult to identify these buried AGNs. So far, it is not clear whether these buried AGNs are luminous enough to detect beneath the heavy starburst activity or whether they are highly obscured by dust. Mid-IR (MIR) spectroscopy and sub-millimetre molecular line observations are useful techniques to differentiate AGN activity from the star-forming regions in nearby ULIRGs (M. Imanishi et al. 2008; P. P. Papadopoulos, K. G. Isaak & P. P. Werf 2010). Radio observations can also play a major role in identifying ULIRGs that host deeply buried AGNs.

Previous studies suggest that ULIRGs are the low-redshift counterpart of submillimetre galaxies and may finally evolve into radio galaxies (R. P. Norris et al. 2012; S. Nandi et al. 2021). Powerful radio galaxies often host peculiar optical interacting systems with tidal tails, bridges of emission, shells, and dust lanes (C. Ramos Almeida et al. 2011). These studies suggest that ULIRGs are the strongest candidates that can connect the evolutionary sequence of mergers and radio galaxies (D. B. Sanders & I. F. Mirabel 1996; A. S. Evans et al. 1999; R. Morganti et al. 2003). The link between radio galaxy and ULIRGs has been identified in few interacting systems (R. Morganti et al. 2004; P. Kukreti et al. 2022). However, the evolution process is still not well known.

Recently, we investigated the evolutionary sequence for the early stages of AGN development in 13 ULIRGs, with a particular focus on gigahertz-peaked spectrum (GPS) sources, compact steep spectrum (CSS) sources or young radio sources (S. Nandi et al. 2021). These classes are widely interpreted as representing early evolutionary phases of radio galaxies, with GPS sources evolving into CSS sources as the radio jets expand within the host galaxy interstellar medium. The typical projected linear size of a GPS source is ≤ 1 kpc and it shows a radio spectrum turnover frequency of ~ 1 GHz. Observations show that the range of the peak frequency of GPS source can vary from 400 MHz to 6 GHz (C. Stanghellini et al. 1998). The peak shifts towards low frequency, as the angular size of the source increases (C. P. O'Dea & D. J. Saikia 2020). A CSS source is $\sim$ 1 to 10 kpc in size and its radio spectrum turns over at a few hundred MHz. Generally, CSS sources peak at frequencies below 400 MHz and exhibit steep radio spectra at high frequencies (C. P. O'Dea & D. J. Saikia 2020). Both classes have symmetric double structure which can be resolved through high-frequency observations. We studied the distribution of the radio flux density of ULIRGs over a wide range of frequencies. We estimated the high-frequency break and low-frequency turnover from their integrated radio spectra. The turnovers at low frequencies are due to synchrotron self-absorption or free–free absorption (M. S. Clemens et al. 2010; T. J. Hayashi, Y. Hagiwara & M. Imanishi 2021). The high-frequency steepening is interpreted as particle energy losses. In our previous work (S. Nandi et al. 2021), the integrated radio spectra of 9 out of 13 ULIRGs derived using archival data and Giant Metrewave Radio Telescope (GMRT) observations, show characteristics that are similar to that of GPS/CSS/young radio sources. The variation of spectral age of these sources is in between 0.4 and 20 Myr. Although this result supports the hypothesis that the ULIRGs are young radio sources, we need a larger population to understand the connection between ULIRGs and radio galaxies which is not statistically clear yet. Thus, studying ULIRGs at radio wavelengths is a way to determine whether these system are progenitors of young radio-loud elliptical galaxies.

In this paper, we investigate a large sample of ULIRGs with multifrequency radio data using new observations from the upgraded GMRT (uGMRT) as well as other ancillary data from different surveys. The paper is arranged as follows. We describe the sample selection process in Section 2. The main methods used to study these sources include modelling the radio spectra and estimating the radio synchrotron age to determine the source's age and characteristics. New observations, data reduction, and archival data availability have been described in Section 3. In Section 4, we describe the results of uGMRT observations, spectra modelling, radio-to-FIR correlation analysis for all sources, the *Wide-field Infrared Survey Explorer* (*WISE*) colour-cut criteria and optical merger classification. In Section 5, we present the discussion of our findings, and in Section 6, we present our final conclusions. We provide a detailed interaction stage classification in Appendix A, highlight the 10 most interesting sources in Appendix B, and Panoramic Survey Telescope and Rapid Response System (Pan-STARRS) images of all sources in Appendix C.

2 SAMPLE SELECTION

We selected our sample from the *IRAS* 1 Jy Survey of ULIRGs (D. C. Kim & D. B. Sanders 1998), which consists of a large sample of 118 sources. We have selected 38 ULIRGs (see Table 1) based on their detection in both National Radio Astronomy Observatory (NRAO) Very Large Array (VLA) Sky Survey (NVSS) and the Tata Institute of Fundamental Research (TIFR) Giant Metrewave Radio Telescope (GMRT) Sky Survey (TGSS). In the first phase of our work, S. Nandi et al. (2021), we examined 13 of these 38 ULIRGs. In this paper, we study the radio spectra of the remaining 25 new sources as well as examine their AGN activity, host galaxy evolution for the sample of 38 sources. The entire sample, along with their right ascension, declination, redshift, and optical nuclear type information, is summarized in Table 1. The sources marked with (♦) represent the 13 ULIRGs analysed in the first phase of this study by S. Nandi et al. (2021). Among our sample, 39.47 per cent exhibit Seyfert 2 characteristics, 10.53 per cent show Seyfert 1 characteristics, 31.58 per cent are classified as LINERs (low-ionization nuclear emission-line regions), and 15.79 per cent display H II region characteristics (see Fig. 1, left panel), which presents these optical nuclear classifications in a bar plot showing their percentage distribution. We detail each method and the morphological, physical, and emission characteristics of all sources in our sample in the following sections.

3 RADIO DATA AND ANALYSIS

This section focuses on a new sample of 25 sources, selected from the total set of 38 sources studied in the second phase of our research. The first phase, which included 13 sources, was previously discussed in S. Nandi et al. (2021). In this second phase, we conducted uGMRT observations and utilized archival data to study the radio spectra of these sources. The details of the uGMRT observations, data reduction, and the availability of archival data are provided below.

3.1 uGMRT observations

From the new sample of 25 sources, we proposed to map the low-frequency radio continuum emission of five ULIRGs: IRAS 05156−3024, IRAS F07599+6508, IRAS 10494+4424, IRAS

Table 1. ULIRGs in the sample and their optical nuclear types.

Galaxy (1)	RA (2)	Dec. (3)	z (4)	Nuclear type (5)
IRAS 00188−0856♦	00h21m26.5s	−08°39′26″	0.128	LINER
IRAS 00456−2904	00h48m06.8s	−28°48′19″	0.109	H II
IRAS F01004−2237†	01h02m50.0s	−22°21′57″	0.118	H II
IRAS 01494−1845†	01h51m51.4s	−18°30′46″	0.158	H II
IRAS 01569−2939	01h59m13.8s	−29°24′35″	0.139	H II
IRAS 01572+0009♦	01h59m50.2s	+00°23′41″	0.163	Seyfert 1
IRAS 02480−3745†	02h50m01.7s	−37°32′45″	0.165	Unclassified
IRAS 04103−2838†	04h12m19.4s	−28°30′25″	0.118	LINER
IRAS 05156−3024	05h17m32.5s	−30°21′13″	0.171	Seyfert 2
IRAS 05189−2524	05h21m01.4s	−25°21′45″	0.044	Seyfert 2
IRAS F07599 + 6508	08h04m33.1s	+64°59′49″	0.148	Seyfert 1
IRAS 08559 + 1053	08h58m41.7s	+10°41′22″	0.148	Seyfert 2
IRAS 10494 + 4424	10h52m23.5s	+44°08′48″	0.092	LINER
IRAS 11095−0238	11h12m03.4s	−02°54′22″	0.106	LINER
IRAS 11119 + 3257	11h14m38.9s	+32°41′33″	0.187	Seyfert 1
IRAS 12032 + 1707	12h05m47.7s	+16°51′08″	0.217	LINER
IRAS 12112 + 0305♦	12h13m46.0s	+02°48′38″	0.073	LINER
IRAS 12127−1412	12h15m18.9s	−14°29′45″	0.133	LINER
IRAS 12265 + 0219	12h29m06.7s	+02°03′09″	0.158	Seyfert 1
IRAS 13305−1739♦	13h33m16.5s	−17°55′11″	0.148	Seyfert 2
IRAS 13335−2612	13h36m22.3s	−26°27′34″	0.125	LINER
IRAS 13428 + 5608	13h44m42.1s	+55°53′13″	0.037	Seyfert 2
IRAS 13443 + 0802	13h46m51.1s	+07°47′19″	0.135	Seyfert 2
IRAS 13451 + 1232	13h47m33.3s	+12°17′24″	0.122	Seyfert 2
IRAS 13539 + 2920	13h56m09.9s	+29°05′35.2″	0.109	H II
IRAS 14060 + 2919	14h08m19.0s	+29°04′47″	0.117	H II
IRAS 14070 + 0525♦	14h09m31.2s	+05°11′31″	0.264	Seyfert 2
IRAS 14394 + 5332♦	14h41m04.4s	+53°20′09″	0.105	Seyfert 2
IRAS 15001 + 1433♦	15h02m31.9s	+14°21′35″	0.162	Seyfert 2
IRAS 15327 + 2340	15h34m57.2s	+23°30′11″	0.018	LINER
IRAS 16155 + 0146♦	16h18m09.4s	+01°39′21″	0.132	Seyfert 2
IRAS 17028 + 5817♦	17h03m41.9s	+58°13′45″	0.106	LINER
IRAS 17044 + 6720♦	17h04m28.4s	+67°16′23″	0.136	LINER
IRAS 17179 + 5444♦	17h18m54.4s	+54°41′48″	0.147	Seyfert 2
IRAS 23060 + 0505♦	23h08m33.9s	+05°21′30″	0.172	Seyfert 2
IRAS 23233 + 2817	23h25m49.4s	+28°34′21″	0.113	Seyfert 2
IRAS F23234 + 0946	23h25m56.2s	+10°02′49″	0.128	LINER
IRAS 23389 + 0300♦	23h41m30.3s	+03°17′26″	0.145	Seyfert 2

Notes. The table presents properties of the ULIRG sample. The columns are as follows: (1) source name: sources marked with (♦): 13 sources were extracted from S. Nandi, M. Das & K. S. Dwarakanath (2021); sources marked with (†) have their spectral indices estimated using two different methods: three sources were fitted with a power-law model using GNUPLOT, while one source had its two-point spectral index calculated; (2) and (3) right ascension and declination were obtained from NASA/IPAC Extragalactic Database (NED); (4) redshift (z); and (5) optical nuclear type classification based on S. Veilleux, D.-C. Kim & D. B. Sanders (2002).

11119+3257, and IRAS 13428 + 5608, under the observation code 40_103.

The observations were carried out using the uGMRT, which was developed to provide wider frequency coverage and substantially improved sensitivity compared to the legacy GMRT system. The upgrade introduced wide-band receiver and backend systems in place of the earlier narrow-band configuration, allowing instantaneous bandwidths of up to 400 MHz and improved dynamic range. In this study, we used uGMRT Band 3 (250–500 MHz) and Band 4 (550–850 MHz). These improvements significantly enhance continuum sensitivity at low radio frequencies, making the uGMRT well suited for probing compact and young radio sources (Y. Gupta & others 2017).

To determine their integrated radio spectra, we conducted band 3 observations for all five sources. Band 4 observations were carried out for four of them, excluding IRAS 11119 + 3257. In addition to our uGMRT observations, we utilized various radio surveys and archival data to achieve broad frequency coverage for these five sources. For the remaining 20 sources, only archival data were used, without any new observations.

The observation dates, primary and phase calibrators, beam sizes, position angles, integration times, and rms noise values for these sources in bands 3 and 4 are provided in Table 2. We performed data reduction using available pipelines to obtain the best possible imaging quality for each source. In general, we used the Source Peeling and Atmospheric Modeling pipeline (SPAM; H. T. Intema 2014), an Astronomical Image Processing System (AIPS)-based PYTHON extension (E. W. Greisen 2003) which performs direction-dependent calibration and applies ionospheric corrections. We also used the Common Astronomy Software Applications package (CASA; B. Bean et al. 2022). For IRAS 13428 + 5608 (observed in both bands 3 and 4), we adopted the CASA

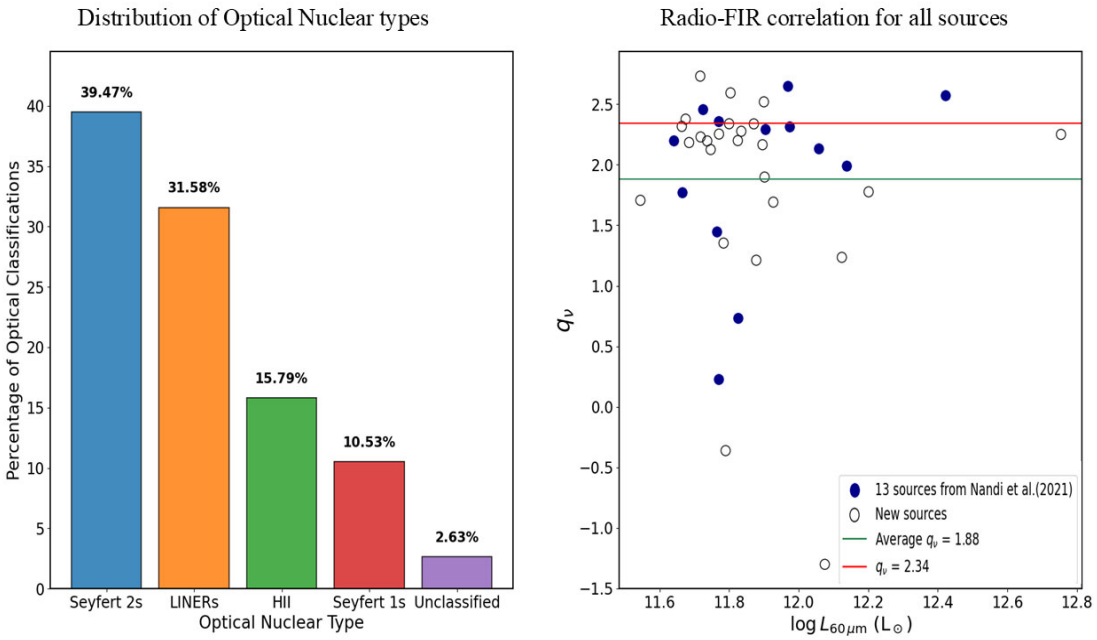

Figure 1. The left panel displays a percentage bar plot illustrating the optical nuclear classification of the complete sample of 38 ULIRGs. The right panel shows a scatter plot of q_ν versus $\log L_{60\,\mu m}$ for the 38 ULIRGs. Filled points indicate the 13 sources from the first phase of this study, taken from S. Nandi et al. (2021). The green line denotes the average q_ν value of 1.88 for the 38 sources in our sample, while the red line marks the $q_\nu = 2.34$ threshold from M. S. Yun, N. A. Reddy & J. J. Condon (2001). Sources below this threshold exhibit characteristics of radio excess, whereas those above the threshold indicate IR excess.

Table 2. uGMRT Band 3 and Band 4 observational details of selected ULIRGs in the sample.

Band 3							
Galaxy (1)	Obs date (2)	Primary calibrator (3)	Phase calibrator (4)	Beam size (‘×’) (5)	PA (°) (6)	Time (min) (7)	rms (mJy beam^{-1}) (8)
IRAS 05156−3024	12-07-2021	3C147, 3C286	0521−207	11.23×4.64	33.55	40	0.064
IRAS F07599+6508	12-07-2021	3C147, 3C286	0834+555	9.05×4.90	42.54	40	0.075
IRAS 10494+4424	12-07-2021	3C147, 3C286	1021+219	9.12×4.59	69.42	40	0.078
IRAS 11119+3257	12-07-2021	3C147, 3C286	1021+219	7.13×4.62	61.68	40	0.105
IRAS 13428+5608	12-07-2021	3C147, 3C286	1459+716	12.89×4.49	75.52	5	0.490
Band 4							
Galaxy (1)	Obs date (2)	Primary calibrator (3)	Phase calibrator (4)	Beam size (‘×’) (5)	PA (°) (6)	Time (min) (7)	rms (mJy beam^{-1}) (8)
IRAS 05156−3024	10-07-2021	3C147, 3C286	0521−207	11.23×4.64	33.55	37	0.089
IRAS F07599+6508	10-07-2021	3C147, 3C286	0834+555	9.05×4.90	42.54	37	0.116
IRAS 10494+4424	10-07-2021	3C147, 3C286	1021+219	9.12×4.59	69.42	32	0.142
IRAS 13428+5608	10-07-2021	3C147, 3C286	1459+716	12.89×4.49	75.52	21	0.216

Notes. The table presents the observation log of ULIRGs at bands 3 and 4. The columns are as follows: (1) source name; (2) observation date; (3) primary calibrator; (4) phase calibrator; (5) synthesized beam size (in arcsec); (6) position angle (PA) in degrees; (7) on-source integration time (minutes); and (8) RMS noise (mJy beam^{-1}).

Pipeline-cum-Toolkit for Upgraded GMRT data Reduction (CAPTURE; R. Kale & C. H. Ishwara-Chandra 2021). This is because the SPAM calibration did not recover any extended emission in this source, while CAPTURE was able to recover faint extended structure, resulting in a higher quality image. Using flux measurements across different frequency bands, we constructed the radio spectra for our sample sources.

3.2 Data reduction using SPAM

For the observed five sources, data reduction was performed using SPAM. The process began with the conversion of raw Long-Term Accumulation (LTA) files into UVFITS format to ensure compatibility with standard interferometric processing tools. Since SPAM cannot process wide-band data in a single step, the data set was automatically divided into multiple sub-bands for independent calibration.

For our observations, five sources were processed in band 3, where the data were split into six sub-bands centred at 450 MHz. Four of these sources were also observed in band 4, and their data were divided into seven sub-bands centred at 650 MHz. This sub-banding approach was necessary to improve calibration accuracy, as SPAM does not support processing large fractional bandwidths ($\Delta f/f > 0.2$) in a single run. Each sub-band underwent

pre-calibration, beginning with initial flagging to remove corrupted data caused by radio frequency interference, malfunctioning antennas, and instrumental errors. Residual instrumental effects were corrected, followed by direction-dependent ionospheric calibration. The final imaging was performed with `WSClean` (A. R. Offringa et al. 2014), a multiscale, multifrequency synthesis deconvolution tool that uses the *w*-stacking algorithm for efficient Fourier transformation. The calibrated visibilities from all sub-bands were combined, converted into measurement sets with CASA, and processed to generate the final continuum image. The final wide-band image, saved as an `*MFS-image.fits*` file, provided a high-resolution map of the radio sources in our sample. This systematic approach ensured precise calibration and high fidelity imaging, improving the accuracy of the uGMRT data for our sources.

3.3 Archival radio data

To determine the integrated radio spectrum of our sample, we utilized various radio surveys and archival data, ensuring broad frequency coverage for all sources. Archival data for the 25 newly selected sources were obtained from multiple surveys that covered a wide range of frequencies and resolutions. Data were obtained from the Very Large Array Low-Frequency Sky Survey Redux at 73.8–74 MHz with an angular resolution of 75 arcsec (W. M. Lane et al. 2014), the Galactic and Extra-Galactic All-Sky MWA Survey at 72–231 MHz with a resolution around 2 arcmin (R. B. Wayth et al. 2015), TGSS at 150 MHz with a resolution of approximately 25 arcsec (H. T. Intema et al. 2017), the 6th Cambridge Survey of Radio Sources at 151 MHz with a resolution of 4.2× 4.2 cosec(Dec.) arcmin^2 (EW× NS) (S. E. G. Hales et al. 1990), and the Westerbork Northern Sky Survey at 325 MHz with a resolution of 54 arcsec (R. B. Rengelink et al. 1997).

Additionally, we used data from the Texas Survey of Discrete Radio Sources at 365 MHz (J. N. Douglas et al. 1996), the Bologna Northern Cross Telescope at 408 MHz (A. Ficarra et al. 1990), the Rapid Australian Square Kilometre Array Pathfinder (ASKAP) Continuum Survey (RACS) at 880–887 MHz with an angular resolution of 25 arcsec (D. McConnell et al. 2020), the Faint Images of the Radio Sky at Twenty-cm at 1400 MHz at resolution of 5 arcsec (D. J. Helfand, R. L. White & R. H. Becker 2015), NVSS at 1400 MHz with a resolution of about 45 arcsec (J. J. Condon et al. 1998), and the Very Large Array Sky Survey (VLASS) at 2–4 GHz with a resolution of 2.5 arcsec (Y. A. Gordon et al. 2021). We also included data from the Green Bank (GB6) Survey at 4850 MHz, which has a resolution of 3 arcmin (P. C. Gregory et al. 1996), along with archival Very Large Array (VLA) images at various frequencies and array configurations. This extensive archival data set provided broad frequency coverage, enabling a detailed analysis of the radio spectra of our sources.

4 RESULTS

4.1 The uGMRT images

We present the band 3 images of five ULIRGs and the band 4 images of four ULIRGs obtained using uGMRT (see Figs 2 and 3). The resulting images, obtained after SPAM processing, not only provide sensitive radio images of the ULIRGs but also reveal minor extended structures, possibly due to radio jets or stellar/AGN outflows. IRAS 05156−3024 does not exhibit any extended structure in either band (Figs 2 and 3). Both IRAS F07599+6508 and IRAS 11119 + 3257 display minor extended radio structures in band 3 (Fig. 2). However, IRAS F07599 + 6508 appears as a point source in band 4 (Fig. 3). The source IRAS 10494 + 4424 appears very compact in both bands (Figs 2 and 3). The source IRAS 13428 + 5608, also known as Mrk 273, is a well-known source that shows extended emission in both bands. A detailed examination of its extended structure requires longer observation times. Large-scale radio emission from this source has already been reported at 144 MHz by P. Kukreti et al. (2022) using Low Frequency Array (LOFAR).

4.2 Radio spectra of new sources in the second phase

Studying the radio spectra of ULIRGs can help answer questions about the physical processes driving their radio emission, such as synchrotron radiation from magnetic fields or emission from ionized gas and dust. Spectral characteristics such as turnover frequencies, spectral breaks, and the slope of the spectrum allow us to distinguish between AGN-driven activity and star formation processes. These features can also provide clues about the evolutionary stage of the ULIRGs, indicating whether the radio emission arises from a young, compact source, an aging electron population, or a system undergoing merger-driven activity. Together, this information helps determine their potential as progenitors of radio galaxies. In this second phase of our study of ULIRG radio emission, we focus on the new sample of 25 ULIRGs. Using uGMRT data along with archival observations covering a wide range of frequencies, we determined the integrated radio spectra for 21 out of the 25 sources. Here, we note that the GMRT beam size and some other low frequency survey beam size is relatively large, compared with that of the very long baseline interferometry (VLBI). So, in a few cases measured radio emission may include contributions from components other than the central source. The flux density measurements and corresponding frequencies used in the spectral fitting are provided in Table 3, along with their associated uncertainties and references. The remaining four sources lacked sufficient data points to perform reliable spectral fitting as indicated by the † in Table 4. We performed radio spectral energy distribution (SED) modelling for these 21 sources using the SYNAGE software (M. Murgia et al. 1999), as shown in Figs 4, 5, 6, and 7. The SYNAGE output parameters, including the injection spectral index ($\alpha_{\rm inj}$), spectral break frequencies, the reduced values χ^2 for the goodness of fit, the magnetic field strengths and the synchrotron ages, are shown in Table 4. Most of the sources in the second phase exhibit a low turnover frequency, ranging from 63 to 383 MHz. To estimate spectral ages and magnetic field strengths, we use the method described in S. Nandi et al. (2021). The spectral ages, estimated using the break frequency, range from 0.0093 to 44 Myr, with eight sources showing very young spectral ages. Furthermore, we observed a very high break frequency for 11 sources. We have calculated upper age limits for these sources. Fig. 7 shows a histogram of synchrotron age estimates for the full sample, including both estimated ages and upper age limits. We computed the spectral index for 3 of these sources by fitting power-law model using `gnuplot`. For the source IRAS 02480−3745, which had only two data points, we performed a two-point spectral index calculation. Using the spectral index information, we have estimated flux density and luminosity for each source at 6 GHz (Table 4). In our sample ∼82 per cent sources are radio quiet with log $L_{6GHz} \lesssim 23.2$ WHz^{-1} (K. I. Kellermann et al. 2016), while only seven sources can be categorized as radio-loud AGNs.

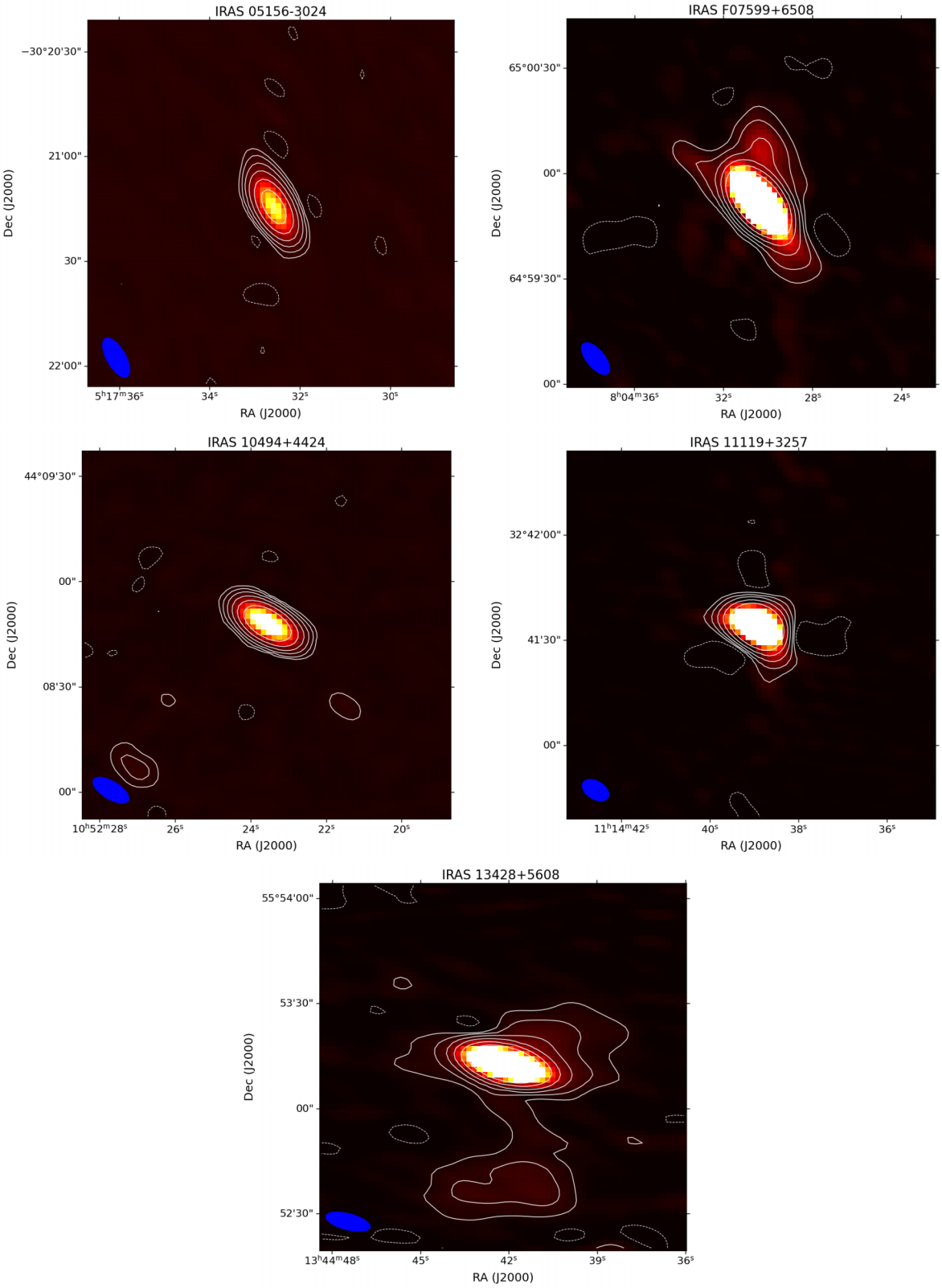

Figure 2. uGMRT Band 3 contour images of the five ULIRGs. Radio contours start at 5σ and increase by factors of 2, where σ represents the local rms noise level: 0.064, 0.075, 0.078, 0.105, and 0.490 mJy beam^{-1} for IRAS 05156−3024, IRAS F07599+6508, IRAS 10494+4424, IRAS 11119+3257, and IRAS 13428 + 5608, respectively.

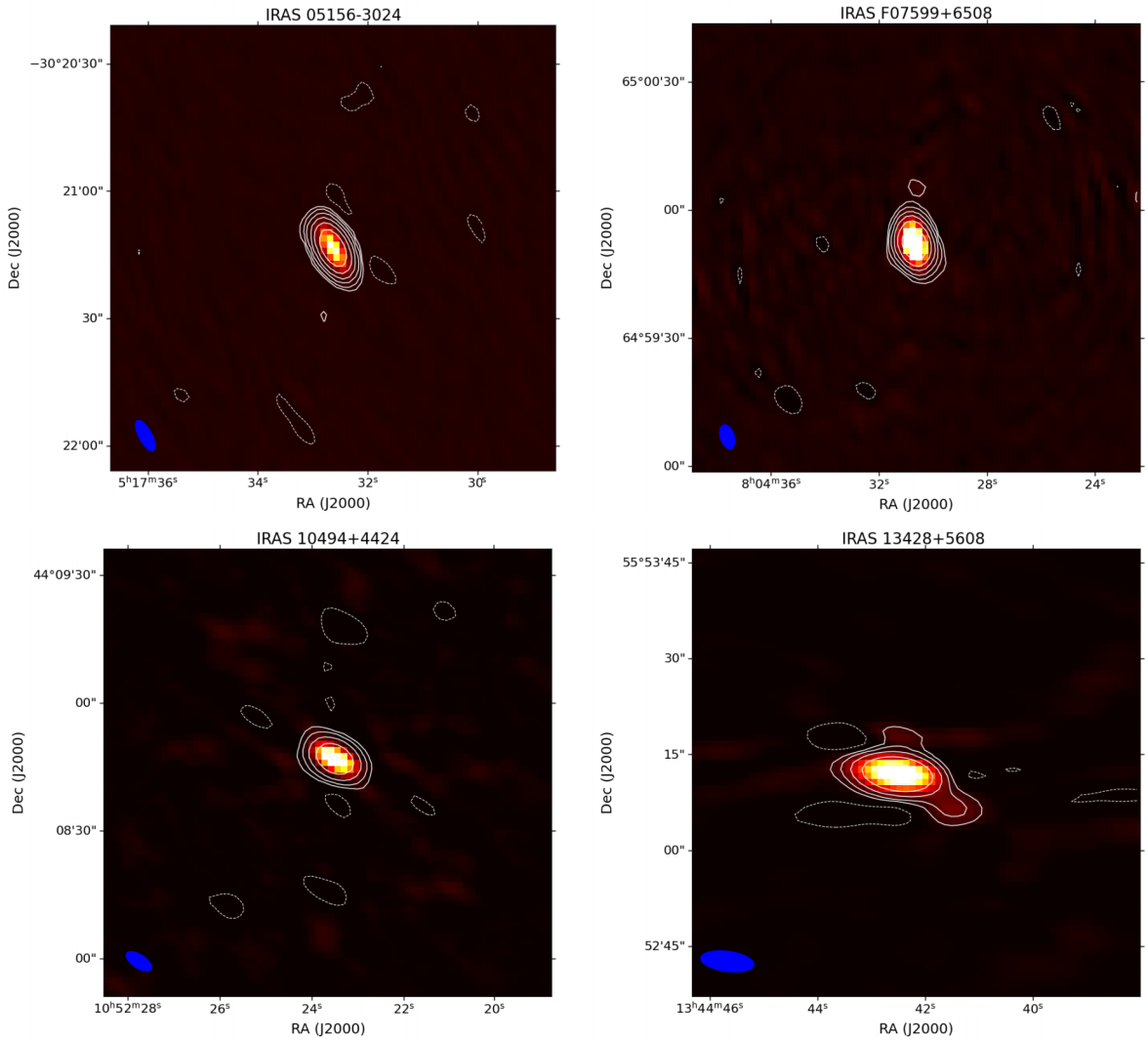

Figure 3. uGMRT Band 4 contour images of the four ULIRGs. Radio contours start at 5σ and increase by factors of 2, where σ represents the local rms noise level: 0.089, 0.116, 0.142, and 0.216 mJy beam^{-1} for IRAS 05156−3024, IRAS F07599+6508, IRAS 10494+4424, and IRAS 13428 + 5608, respectively.

4.3 Radio–FIR correlation

An analysis of radio–FIR correlation was conducted to identify whether the sources show characteristics of starbursts or AGN (M. S. Yun et al. 2001). This correlation reflects the connection between radio and FIR emissions due to star formation in the galaxy. Relativistic electrons in supernova remnants produce non-thermal synchrotron emission, while short-lived massive stars generate these remnants. These stars also emit in the FIR due to re-radiation by dust heated by ultraviolet (UV) emission (A. Basu, S. Roy & D. Mitra 2012). Non-linearity in the correlation may arise if the radio luminosity is not proportional to the star formation activity. The degree of dispersion or non-linearity can be quantified using the 'q_ν' parameter (logarithmic FIR-to-radio flux density ratio) as described by J. J. Condon et al. (1990), and J. J. Condon, M. L. Anderson & G. Helou (1991). In the *IRAS* 2 Jy sample (M. S. Yun et al. 2001), the mean 'q_ν' value is approximately 2.34. The points below $q_\nu = 2.34$ signify radio-dominated emission, and those above indicate IR-dominated emission. We carried out this analysis at the 1.4 GHz frequency band, as the flux density at this frequency is available for all the sources. The 1.4 GHz luminosity was calculated using the following relation:

$$\log L_{1.4\,\mathrm{GHz}}(\mathrm{W\,Hz^{-1}}) = 20.08 - 2\log D + \log S_{1.4\,\mathrm{GHz}} \quad (1)$$

where D is the distance in Mpc and $S_{1.4\,\mathrm{GHz}}$ is the flux density in units of Jy. Similarly, we estimated the luminosity at 60 μm using the following relation:

$$\log L_{60\mu\mathrm{m}}(\mathrm{L_\odot}) = 6.014 - 2\log D + \log S_{60\mu\mathrm{m}} \quad (2)$$

According to G. Helou, B. T. Soifer & M. Rowan-Robinson (1985)and T. J. Hayashi et al. (2021), the correlation between the radio and FIR luminosity, denoted as q_ν, is given by the following equation:

$$q_\nu = \log\left[\left(\frac{f_{\mathrm{FIR}}}{3.75\times10^{12}\ \mathrm{Hz}}\right)/f_\nu\right] \quad (3)$$

where f_{FIR} is the FIR flux density in units of W m^{-2}Hz^{-1} commonly defined as,

$$f_{\mathrm{FIR}} = 1.26\times10^{14}\,(2.58\times f_{60} + f_{100}) \quad (4)$$

Table 3. Observed flux densities at various radio frequencies with associated errors for ULIRGs in the sample.

Galaxy	Frequency (MHz)	Flux density (mJy)	Flux density error (mJy)	Reference
(1)	(2)	(3)	(4)	(5)
IRAS 00456−2904	150	29.252	2.925	H. T. Intema et al. (2017)
	887	26.000	2.320	C. L. Hale et al. (2021)
	1400	21.400	0.642	J. J. Condon et al. (1998)
	3000	12.943	0.388	Y. A. Gordon et al. (2021)
IRAS F01004−2237†	887	20.000	1.900	D. McConnell et al. (2020)
	1400	13.700	0.600	J. J. Condon et al. (1998)
	1400	13.400	0.402	D. J. Helfand et al. (2015)
	3000	4.367	0.131	Y. A. Gordon et al. (2021)
IRAS 01494−1845†	887	11.900	1.190	D. McConnell et al. (2020)
	1400	8.000	0.240	J. J. Condon et al. (1998)
	3000	4.902	0.147	Y. A. Gordon et al. (2021)
IRAS 01569−2939	74	782.800	84.960	W. M. Lane et al. (2014)
	88	661.780	70.140	R. B. Wayth et al. (2015)
	150	578.860	57.880	H. T. Intema et al. (2017)
	155	498.670	52.850	R. B. Wayth et al. (2015)
	200	456.610	48.400	R. B. Wayth et al. (2015)
	800	177.600	12.930	C. L. Hale et al. (2021)
	1400	123.900	3.710	J. J. Condon et al. (1998)
	3000	59.870	1.790	Y. A. Gordon et al. (2021)
	1510	110.410	11.040	VLA archival image
	1510	105.790	10.580	VLA archival image
	1510	98.230	9.820	VLA archival image
	8460	12.880	0.610	VLA archival image
IRAS 02480−3745†	150	98.880	9.888	H. T. Intema et al. (2017)
	1400	13.100	0.393	J. J. Condon et al. (1998)
IRAS 04103−2838†	150	35.020	3.502	H. T. Intema et al. (2017)
	887	19.240	1.846	D. McConnell et al. (2020)
	1400	13.700	0.240	J. J. Condon et al. (1998)
	3000	8.173	0.245	Y. A. Gordon et al. (2021)
IRAS 05156−3024	150	128.290	12.890	H. T. Intema et al. (2017)
	200	62.650	6.640	R. B. Wayth et al. (2015)
	402	37.100	1.850	This work
	745	26.310	1.310	This work
	800	23.000	2.110	D. McConnell et al. (2020)
	834	19.800	1.850	T. Mauch et al. (2013)
	1400	18.700	0.560	J. J. Condon et al. (1998)
	3000	11.490	0.340	Y. A. Gordon et al. (2021)
	3000	12.640	0.370	Y. A. Gordon et al. (2021)
IRAS 05189−2524	150	27.560	2.560	H. T. Intema et al. (2017)
	800	31.600	2.710	D. McConnell et al. (2020)
	1400	29.100	0.870	J. J. Condon et al. (1998)
	1430	27.110	2.710	VLA archival image
	1450	22.880	0.810	VLA archival image
	1510	29.080	2.910	VLA archival image
	1690	26.000	2.600	VLA archival image
	3000	22.980	0.680	Y. A. Gordon et al. (2021)
	4890	11.700	2.900	VLA archival image
	8490	7.780	0.390	VLA archival image
	8490	8.320	0.420	VLA archival image
	8490	10.040	0.500	VLA archival image
IRAS F07599 + 6580	150	151.970	15.190	H. T. Intema et al. (2017)
	325	129.740	0.130	R. B. Rengelink et al. (1997)
	408	91.200	4.560	This work
	745	60.700	3.320	This work
	1400	41.760	1.250	J. J. Condon et al. (1998)
	1450	39.150	1.390	VLA archival image
	1510	32.250	3.220	VLA archival image
	4890	9.590	0.690	VLA archival image
	8460	5.970	0.590	VLA archival image
	14900	2.450	0.480	VLA archival image
	15000	2.900	0.130	N. M. Nagar et al. (2003)

Table 3 – *continued*

Galaxy	Frequency (MHz)	Flux density (mJy)	Flux density error (mJy)	Reference
(1)	(2)	(3)	(4)	(5)
IRAS 08559 + 1053	150	42.127	4.212	H. T. Intema et al. (2017)
	887	17.500	1.725	D. McConnell et al. (2020)
	1400	12.200	0.366	J. J. Condon et al. (1998)
	1400	12.720	0.381	Y.-T. Lin, H.-J. Huang & Y.-C. Chen (2018)
	3000	6.685	0.200	Y. A. Gordon et al. (2021)
	3000	7.126	0.213	Y. A. Gordon et al. (2021)
IRAS 10494 + 4424	150	43.480	4.340	H. T. Intema et al. (2017)
	325	43.420	0.550	R. B. Rengelink et al. (1997)
	402	31.680	1.590	This work
	745	50.000	2.500	This work
	1400	22.400	0.670	J. J. Condon et al. (1998)
	1400	24.200	0.720	D. J. Helfand et al. (2015)
	1490	22.520	0.670	VLA archival image
	3000	14.820	0.440	Y. A. Gordon et al. (2021)
	15000	2.800	0.140	N. M. Nagar et al. (2003)
IRAS 11095−0238	150	58.710	5.871	H. T. Intema et al. (2017)
	887	39.000	3.230	D. McConnell et al. (2020)
	1400	25.100	0.753	J. J. Condon et al. (1998)
	1400	19.780	0.593	D. J. Helfand et al. (2015)
	3000	11.724	0.351	Y. A. Gordon et al. (2021)
IRAS 11119 + 3257	150	158.000	15.800	H. T. Intema et al. (2017)
	402	298.800	14.940	This work
	1400	110.400	3.310	J. J. Condon et al. (1998)
	1400	105.350	3.160	D. J. Helfand et al. (2015)
	1400	108.240	3.240	D. J. Helfand et al. (2015)
	2200	46.000	4.600	L. Petrov (2013)
	2300	50.000	5.000	G. Bourda et al. (2010)
	3000	45.970	1.370	Y. A. Gordon et al. (2021)
	8400	5.000	0.500	G. Bourda et al. (2010)
	8460	9.820	0.980	G. Bourda et al. (2010)
IRAS 12032 + 1707	150	90.228	9.022	H. T. Intema et al. (2017)
	887	41.000	3.370	D. McConnell et al. (2020)
	1400	29.310	0.879	D. J. Helfand et al. (2015)
	1400	28.400	0.852	J. J. Condon et al. (1998)
	3000	14.902	0.447	Y. A. Gordon et al. (2021)
	15 000	1.900	0.095	N. M. Nagar et al. (2003)
IRAS 12127−1412	118	20.000	2.120	R. B. Wayth et al. (2015)
	150	126.690	12.660	H. T. Intema et al. (2017)
	155	80.000	8.480	R. B. Wayth et al. (2015)
	200	112.000	11.870	R. B. Wayth et al. (2015)
	800	114.000	8.480	D. McConnell et al. (2020)
	1400	76.000	2.280	J. J. Condon et al. (1998)
	3000	49.420	1.480	Y. A. Gordon et al. (2021)
IRAS 12265 + 0219 (3C273)	73.8	170340.000	19044.000	W. M. Lane et al. (2014)
	150	119198.000	11919.800	H. T. Intema et al. (2017)
	887	65020.000	4551.900	D. McConnell et al. (2020)
	1400	5499.2	110.950	D. J. Helfand et al. (2015)
	3000	38611.500	1158.340	Y. A. Gordon et al. (2021)
	15 000	21614.000	1028.830	N. M. Nagar et al. (2003)
	22000	41000.000	28700.000	W. K. Gear et al. (1994)
IRAS 13335−2612	150	40.273	4.027	H. T. Intema et al. (2017)
	887	20.000	1.900	D. McConnell et al. (2020)
	1400	12.600	0.378	J. J. Condon et al. (1998)
	3000	9.364	0.280	Y. A. Gordon et al. (2021)
IRAS 13428 + 5608	74	405.000	45.270	W. M. Lane et al. (2014)
	150	366.600	36.660	T. W. Shimwell et al. (2017)
	151	580.000	90.000	S. E. G. Hales et al. (1990)
	244	394.000	20.000	M. S. Clemens et al. (2010)
	365	335.000	37.000	J. N. Douglas et al. (1996)
	402	318.810	15.940	This work
	610	222.000	8.000	M. S. Clemens et al. (2010)

Table 3 – *continued*

Galaxy	Frequency (MHz)	Flux density (mJy)	Flux density error (mJy)	Reference
(1)	(2)	(3)	(4)	(5)
	745	180.190	9.000	This work
	1380	126.630	12.660	VLA archival image
	1380	152.760	15.280	VLA archival image
	1400	145.400	5.200	J. J. Condon et al. (1998)
	1400	132.000	3.960	F. M. Maccagni et al. (2017)
	1400	163.000	4.890	M. J. I. Brown et al. (2017)
	1430	138.460	13.850	VLA archival image
	1450	139.340	4.950	VLA archival image
	1510	98.510	9.850	VLA archival image
	1510	102.580	0.260	VLA archival image
	1510	139.390	13.940	VLA archival image
	1690	108.560	10.860	VLA archival image
	2700	96.000	6.000	R. A. Sramek & H. M. Tovmassian (1976)
	3000	100.000	3.000	Y. A. Gordon et al. (2021)
	4755	73.000	5.000	M. D. Bicay et al. (1995)
	4850	99.000	14.850	R. H. Becker, R. L. White & A. L. Edwards (1991)
	4850	103.000	12.000	P. C. Gregory & J. J. Condon (1991)
	4890	35.870	2.590	VLA archival image
	4890	67.500	4.880	VLA archival image
	4890	63.100	4.560	VLA archival image
	4890	68.280	4.970	VLA archival image
	5000	70.000	14.000	G. Kojoian et al. (1980)
	5010	40.890	4.090	VLA archival image
	5950	60.300	0.080	A. K. Leroy et al. (2011)
	8100	41.000	5.000	R. A. Sramek & H. M. Tovmassian (1976)
	8460	29.390	1.850	VLA archival image
	8460	27.410	1.730	VLA archival image
	10630	39.000	7.000	M. D. Bicay et al. (1995)
	14900	22.460	1.100	VLA archival image
	15000	18.800	0.940	N. M. Nagar et al. (2003)
	22500	14.300	0.300	M. S. Clemens et al. (2008)
IRAS 13443 + 0802	150	26.780	2.678	H. T. Intema et al. (2017)
	887	16.300	1.641	D. McConnell et al. (2020)
	1400	10.500	0.315	J. J. Condon et al. (1998)
	1400	10.090	0.302	D. J. Helfand et al. (2015)
	3000	6.313	0.189	Y. A. Gordon et al. (2021)
	15 000	1.300	0.062	N. M. Nagar et al. (2003)
IRAS 13451+1232 (PKS 1345 + 12)	150	4036.980	403.698	H. T. Intema et al. (2017)
	178	4600.000	125.000	J. F. R. Gower, P. F. Scott & D. Wills (1967)
	302	7860.000	300.000	C. Stanghellini et al. (1998)
	333	8390.000	300.000	C. Stanghellini et al. (1998)
	365	8309.000	169.000	J. N. Douglas et al. (1996)
	408	8780.000	270.000	C. Stanghellini et al. (1998)
	468	8720.000	850.000	H. Kuehr et al. (1981)
	635	7970.000	330.000	H. Kuehr et al. (1981)
	750	6900.000	200.000	H. Kuehr et al. (1981)
	887	6551.000	161.916	D. McConnell et al. (2020)
	1335	5330.000	150.000	C. Stanghellini et al. (1998)
	1400	5397.200	161.900	J. J. Condon et al. (1998)
	1400	4859.880	145.796	D. J. Helfand et al. (2015)
	1660	4734.000	150.000	C. Stanghellini et al. (2005)
	2695	3600.000	290.000	R. L. Adgie, J. H. Crowther & H. Gent (1972)
	2700	3880.000	128.103	A. Wright & R. Otrupcek (1990)
	3000	4660.200	139.805	Y. A. Gordon et al. (2021)
	3000	4270.110	111.450	Y. A. Gordon et al. (2021)

Table 3 – *continued*

Galaxy	Frequency (MHz)	Flux density (mJy)	Flux density error (mJy)	Reference
(1)	(2)	(3)	(4)	(5)
	4535	3180.000	100.000	C. Stanghellini et al. (1998)
	4850	3092.000	427.000	P. C. Gregory & J. J. Condon (1991)
	5000	2810.000	200.000	H. Kuehr et al. (1981)
	8000	2460.000	369.000	M. A. Stull (1971)
	8085	2280.000	70.000	C. Stanghellini et al. (1998)
	8400	2210.000	70.000	C. Stanghellini et al. (1998)
	10695	1720.000	10.000	H. Kuehr et al. (1981)
	15 000	1475.000	73.750	N. M. Nagar et al. (2003)
	22000	1130.000	90.000	C. Stanghellini et al. (1998)
IRAS 13539 + 2920	150	31.415	3.141	H. T. Intema et al. (2017)
	1400	12.100	0.360	J. J. Condon et al. (1998)
	1400	11.600	0.348	Y.-T. Lin et al. (2018)
	1400	10.700	0.321	R. H. Becker, R. L. White & D. J. Helfand (1995)
	3000	6.020	0.180	Y. A. Gordon et al. (2021)
	15 000	3.100	0.155	N. M. Nagar et al. (2003)
IRAS 14060 + 2919	887	15.000	1.550	D. McConnell et al. (2020)
	1400	9.300	0.279	Y.-T. Lin et al. (2018)
	1400	7.860	0.235	R. H. Becker et al. (1995)
	1400	7.910	0.237	J. J. Condon et al. (1998)
	3000	5.666	0.169	Y. A. Gordon et al. (2021)
IRAS 15327 + 2340 (Arp 220)	150	440.3	44.7	H. T. Intema et al. (2017)
	151	450.000	81.000	E. Waldram et al. (1996)
	365	435.000	26.000	J. N. Douglas et al. (1996)
	887	364.000	25.980	D. McConnell et al. (2020)
	1100	360.000	20.000	P. K. Williams & G. C. Bower (2010)
	1100	340.000	10.000	P. K. Williams & G. C. Bower (2010)
	1200	330.000	10.000	P. K. Williams & G. C. Bower (2010)
	1200	370.000	20.000	P. K. Williams & G. C. Bower (2010)
	1400	373.000	11.190	J. J. Condon et al. (1998)
	1400	326.300	9.789	J. Allison, E. Sadler & A. Meekin (2014)
	1400	320.000	10.000	P. K. Williams & G. C. Bower (2010)
	1500	260.000	20.000	P. K. Williams & G. C. Bower (2010)
	1600	310.000	30.000	P. K. Williams & G. C. Bower (2010)
	1700	300.000	10.000	P. K. Williams & G. C. Bower (2010)
	1800	310.000	10.000	P. K. Williams & G. C. Bower (2010)
	1900	300.000	10.000	P. K. Williams & G. C. Bower (2010)
	2000	300.000	10.000	P. K. Williams & G. C. Bower (2010)
	2380	312.000	16.000	L. Dressel & J. Condon (1978)
	2500	290.000	10.000	P. K. Williams & G. C. Bower (2010)
	2500	270.000	20.000	P. K. Williams & G. C. Bower (2010)
	2600	280.000	20.000	P. K. Williams & G. C. Bower (2010)
	2695	279.000	22.000	J. W. Sulentic (1976)
	2695	260.000	10.000	J. Condon et al. (1983)
	2900	270.000	10.000	P. K. Williams & G. C. Bower (2010)
	3000	279.062	8.371	Y. A. Gordon et al. (2021)
	3000	291.954	8.758	Y. A. Gordon et al. (2021)
	3200	270.000	10.000	P. K. Williams & G. C. Bower (2010)
	3300	270.000	10.000	P. K. Williams & G. C. Bower (2010)
	3400	280.000	10.000	P. K. Williams & G. C. Bower (2010)
	3500	270.000	10.000	P. K. Williams & G. C. Bower (2010)
	3600	240.000	10.000	P. K. Williams & G. C. Bower (2010)
	4300	250.000	20.000	P. K. Williams & G. C. Bower (2010)
	4400	230.000	20.000	P. K. Williams & G. C. Bower (2010)
	4500	240.000	20.000	P. K. Williams & G. C. Bower (2010)
	4600	240.000	20.000	P. K. Williams & G. C. Bower (2010)
	4700	260.000	20.000	P. K. Williams & G. C. Bower (2010)
	4850	204.000	27.000	P. C. Gregory & J. J. Condon (1991)
	5000	192.000	29.000	J. W. Sulentic (1976)

Table 3 – *continued*

Galaxy	Frequency (MHz)	Flux density (mJy)	Flux density error (mJy)	Reference
(1)	(2)	(3)	(4)	(5)
	5000	230.000	10.000	P. K. Williams & G. C. Bower (2010)
	5000	240.000	20.000	P. K. Williams & G. C. Bower (2010)
	5200	230.000	10.000	P. K. Williams & G. C. Bower (2010)
	5400	240.000	10.000	P. K. Williams & G. C. Bower (2010)
	5700	200.000	20.000	P. K. Williams & G. C. Bower (2010)
	5950	194.500	8.000	A. K. Leroy et al. (2011)
	6000	220.000	10.000	P. K. Williams & G. C. Bower (2010)
	6200	290.000	30.000	P. K. Williams & G. C. Bower (2010)
	6300	200.000	30.000	P. K. Williams & G. C. Bower (2010)
	6700	230.000	30.000	P. K. Williams & G. C. Bower (2010)
	7000	190.000	20.000	P. K. Williams & G. C. Bower (2010)
	8085	170.000	20.000	J. Condon et al. (1983)
IRAS 23233 + 2817	150	101.970	10.197	H. T. Intema et al. (2017)
	887	48.000	3.860	D. McConnell et al. (2020)
	1400	35.500	1.200	J. J. Condon et al. (1998)
	1400	35.100	1.053	D. J. Helfand et al. (2015)
	3000	19.221	0.576	Y. A. Gordon et al. (2021)
IRAS F23234 + 0946	150	39.140	3.914	H. T. Intema et al. (2017)
	887	14.000	1.480	D. McConnell et al. (2020)
	1400	11.600	1.000	J. J. Condon et al. (1998)
	1400	10.900	0.327	D. J. Helfand et al. (2015)
	3000	7.527	0.225	Y. A. Gordon et al. (2021)
	15 000	2.400	0.120	N. M. Nagar et al. (2003)

Notes. The table presents flux density measurements for the ULIRGs in our sample at multiple radio frequencies. The columns are as follows: (1) source name; (2) observing frequency in MHz; (3) measured flux density in milliJanskys (mJy); (4) associated uncertainty in flux density (mJy); and (5) reference for the measurement, including published surveys, VLA archival images, and this work.

The radio flux densities at 1.4 GHz (f_ν) and their associated errors, estimated from radio images, along with the flux densities and errors at 60 and 100 μm, were collected from M. Moshir & others (1990). The FIR-to-radio ratios at 1.4 GHz and the corresponding values of q_ν for the 38 sources are tabulated in Table 5. IRAS 12265 + 0219 stands out as the most luminous source in our sample, with $\log L_{1.4\mathrm{GHz}} = 29.397\,\mathrm{WHz}^{-1}$ followed by IRAS 13451 + 1232, which has $\log L_{1.4\mathrm{GHz}} = 28.311\,\mathrm{WHz}^{-1}$. The estimated values of q_ν for these two sources are −1.22 and −0.361, respectively. The right panel of Fig. 1 displays a scatter plot of q_ν values versus $\log(L_{60\,\mu\mathrm{m}})$ for all 38 ULIRGs, with filled circles indicating the 13 sources from the first phase of this study (S. Nandi et al. 2021). The green horizontal line represents the average q_ν value of 1.88, while the red line marks the M. S. Yun et al. (2001) threshold of $q_\nu = 2.34$, below which sources are classified as radio excess and above which they exhibit IR-excess characteristics. Approximately 80 per cent exhibit radio-excess characteristics with $q_\nu < 2.34$.

In Fig. 8, the layout of the first and second panels illustrates the relationship between the radio–IR flux ratio (q_ν) and the luminosity log(60 μm) for the 38 sources in our sample. The first panel presents scatter points colour-mapped by radio synchrotron age, while the second panel displays scatter points categorized by turnover frequency. The third panel is a histogram showing the number of sources in the sample that exhibit turnover characteristics. Out of the 38 sources, 30 sources with estimated radio spectral ages are represented by filled circles, and colour-mapped according to their ages. The remaining eight sources, for which age estimates could not be obtained, are shown as hollow squares. Among the 30 sources with age estimates, 25 (83.3 per cent) exhibit $q_\nu < 2.34$. Of these 25 sources, most sources (64.0 per cent) appear blue in the age colour map, indicating younger spectral ages. This suggests that a significant fraction of the radio-excess sources with spectral age estimates, are in an early evolutionary stage.

The second panel presents a scatter plot of turnover frequencies for all 38 sources. Most of the radio-excess AGNs identified in the first panel also show a low-frequency turnover, indicating their young age. There are eight sources that exhibit IR-excess characteristics, defined by $q_\nu > 2.34$. Among these, six sources appear blue in the first panel, suggesting young spectral ages. Interestingly, these same six sources display very low turnover frequencies in the second panel, which was unexpected.

The third panel shows a histogram of the turnover frequencies, providing a clearer view of the overall distribution corresponding to the scatter plot in the second panel. It reveals that 17 sources in our sample exhibit turnover characteristics.

4.4 Optical interaction class and analysis of *WISE* data

The interaction stage of each ULIRG in our sample is classified as pre-merger, merger, or post-merger based on the optical morphological criteria of S. Veilleux et al. (2002). A detailed description of the classification scheme is provided in Appendix A. The interaction class assigned to each source is listed in Table 6, and the Pan-STARRS optical images illustrating these stages are shown in Figs C1 and C2 in Appendix C. Following the classification of sources based on their optical interaction stages, we investigated their mid-IR properties using data from the *WISE*. We cross-matched the source positions with the *WISE* catalogue and found that 37 out of 38 sources in our sample are detected. The only exception is IRAS F07599 + 6508, which is not detected in *WISE*. *WISE* employs a straightforward method to identify AGN based on the $W1-W2$ colour-cut criterion. According to L. Blecha et

Table 4. SYNAGE output parameters, estimated magnetic fields, synchrotron ages, and logarithmic luminosities at 6 GHz for the ULIRGs in the sample.

Galaxy	α_{inj}	ν_{br} (GHz)	χ^2_{red}	B (nT)	τ_{syn} (Myr)	ν_{max} (MHz)	$\log L_{6\,GHz}$ (W Hz^{-1})
(1)	(2)	(3)	(4)	(5)	(6)	(7)	(8)
IRAS 00188−0856♦	−0.533	5.38	1.03	2.8	4.3	263	22.51
IRAS 00456−2904	−0.375	2.236	1.000	1.004	27	276.5	22.64
IRAS F01004−2237†	−0.980						22.34
IRAS 04194−1845†	−0.661						22.19
IRAS 01569−2939	−0.613	1.703	5.162	1.39	20	63.49	23.57
IRAS 01572 + 0009♦	−0.757	24.6	16.44	4.8	0.87		22.81
IRAS 02480−3745†	−0.891						22.42
IRAS 04103−2838†	−0.2304						22.53
IRAS 05156−3024	−0.582	> 100	6.375	0.97	<23		22.81
IRAS 05189−2524	−0.375	4.317	12.92	5.2	1.9	361.1	21.87
IRAS F07599 + 6508	−0.671	2.156	6.448	28.5	0.21	187.6	22.96
IRAS 08559 + 1053	−0.375	1.039	1.120	0.8	44		22.61
IRAS 10494 + 4424	−0.528	3.824	17.47	24.8	0.19	207.7	22.34
IRAS 11095−0238	−0.850	> 100	11.79	1.16	<19	224.0	22.31
IRAS 11119 + 3257	−1.000	1.638	2.187	13.4	0.73	382.6	23.40
IRAS 12032 + 1707	−0.770	4.503	3.597	26	0.16	213.5	23.10
IRAS 12112 + 0305♦	−0.546	> 100	1.929	4.34	<1.12	290	22.14
IRAS 12127−1412	−0.593	> 100	9.807	1.25	<23	318.5	23.17
IRAS 12265 + 0219	−0.375	> 100	2.063	105	<0.0093		26.33
IRAS 13305−1739♦	−0.591	1.76	0.95	1.4	20		23.07
IRAS 13335−2612	−0.476	> 100	6.693	0.74	<32		22.40
IRAS 13428 + 5608	−0.450	4.891	13.44	3.4	3.5	115.7	22.38
IRAS 13443 + 0802	−0.417	1.997	6.075	18	0.43		22.43
IRAS 13451 + 1232	−0.375	7.666	5.198	18.6	0.21	359.1	25.07
IRAS 13539 + 2920	−0.570	> 100	18.86	23	<0.107		22.19
IRAS 14060 + 2919	−0.525	> 100	13.49	0.63	<39		22.17
IRAS 14070 + 0525♦	−0.775						22.54
IRAS 14394 + 5332♦	−0.768	>100	24.03	4.07	<1.5		22.58
IRAS 15001 + 1433♦	−0.513	12.40	0.28	10.39	0.40		22.76
IRAS 15327 + 2340	−0.375	> 100	2.638	80	<0.76	291.2	22.13
IRAS 16156 + 0146♦	−0.297						22.39
IRAS 17028 + 5817♦	−0.665	2.30	2.01	2.43	8.10	299	22.21
IRAS 17044 + 6720♦	−0.254						22.22
IRAS 17179 + 5444♦	−0.734	5.29	2.29	5.9	1.4	509	23.82
IRAS 23060 + 0505♦	−0.451						22.44
IRAS 23233 + 2817	−0.375	1.215	0.9466	1.0	35		22.82
IRAS F23234 + 0946	−0.498	16.343	1.075	19	<0.14		23.38
IRAS 23389 + 0300♦	−0.740	2.5	3.630	12.4	0.66	177	24.21

Notes. The table presents derived physical properties of the ULIRG sample. The columns are as follows: (1) source name: sources marked with (♦): 13 sources were extracted from the first phase study by S. Nandi et al. (2021); sources marked with (†) have their spectral indices estimated using two different methods: three sources were fitted with a power-law model using GNUPLOT, while one source had its two-point spectral index calculated; (2) injection spectral index; (3) spectral break frequencies in GHz; (4) reduced χ^2 values for the goodness of fit; (5) magnetic fields in nT; (6) synchrotron age in Myr; (7) low-frequency turnover in MHz; and (8) logarithmic radio luminosity at 6 GHz in units of W Hz^{-1}.

al. (2018), galaxies with a $W1-W2$ colour below 0.5 are classified as blue, suggesting potential starburst activity. A colour between 0.51 and 0.8 suggests a possible presence of AGN (pre-merger phase), while a colour greater than 0.8 confirms AGN activity (merger or post-merger phase). We applied this colour-cut criterion to our sample and tabulated the magnitudes $W1$ and $W2$ for all sources in Table 6. To analyse the IR colour properties of our sample, we examined the $W1-W2$ colour index. We found that four sources IRAS 13443+0802, IRAS 13451+1232, IRAS 17044+6720, and IRAS F23234 + 0946 have binary detections in *WISE*. For these sources, *WISE* provides two separate detections at the same RA and Dec. coordinates, each with its own $W1$ and $W2$ magnitudes. As a result, we obtained two different $W1-W2$ values for each of these sources. Among binary-detected sources, we found that two have at least one $W1-W2$ value ≤ 0.5. Based on the classification by L. Blecha et al. (2018) and R. J. Assef et al. (2013), most of the sources in our sample exhibit characteristics indicative of mid-IR AGNs (see Fig. 9).

In Fig. 9, we present a multipanel illustration of the *WISE* colour analysis in relation to various properties of our sample. The first panel displays a scatter plot illustrates the distribution of q_ν values plotted against the logarithm of luminosity at 60 μm for our sample. The scatter data points are colour-coded based on MIR *WISE* colour-selection criteria. Upward and downward triangles denote sources detected as binaries in the *WISE* catalogue, located at identical RA and Dec. coordinates. The source IRAS F07599 + 6508, which is not detected in *WISE,* is marked by a hollow square. The red line in this plot is the average q_ν value of 2.34.

The second panel presents scatter plot of synchrotron spectral age versus *WISE*$W1-W2$ colour. Points are colour-coded such that blue indicates $W1-W2 \leq 0.8$, which typically suggests either star-forming galaxies or obscured AGN activity, while

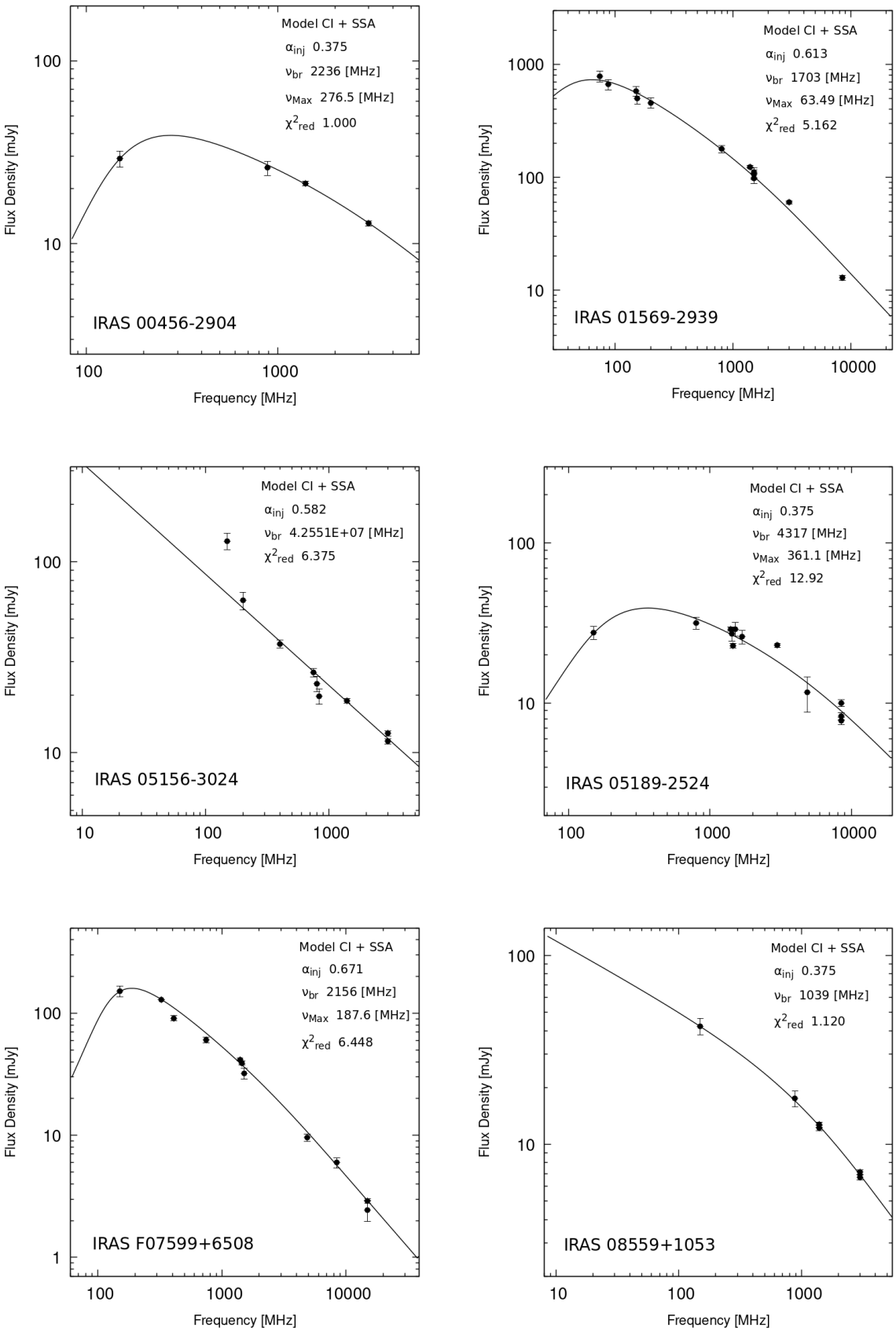

Figure 4. Radio spectra modelled using SYNAGE. Panels show the SEDs for IRAS 00456−2904, IRAS 01569−2939, IRAS 05156−3024, IRAS 05189−2524, IRAS F07599+6508, and IRAS 08559+1053.

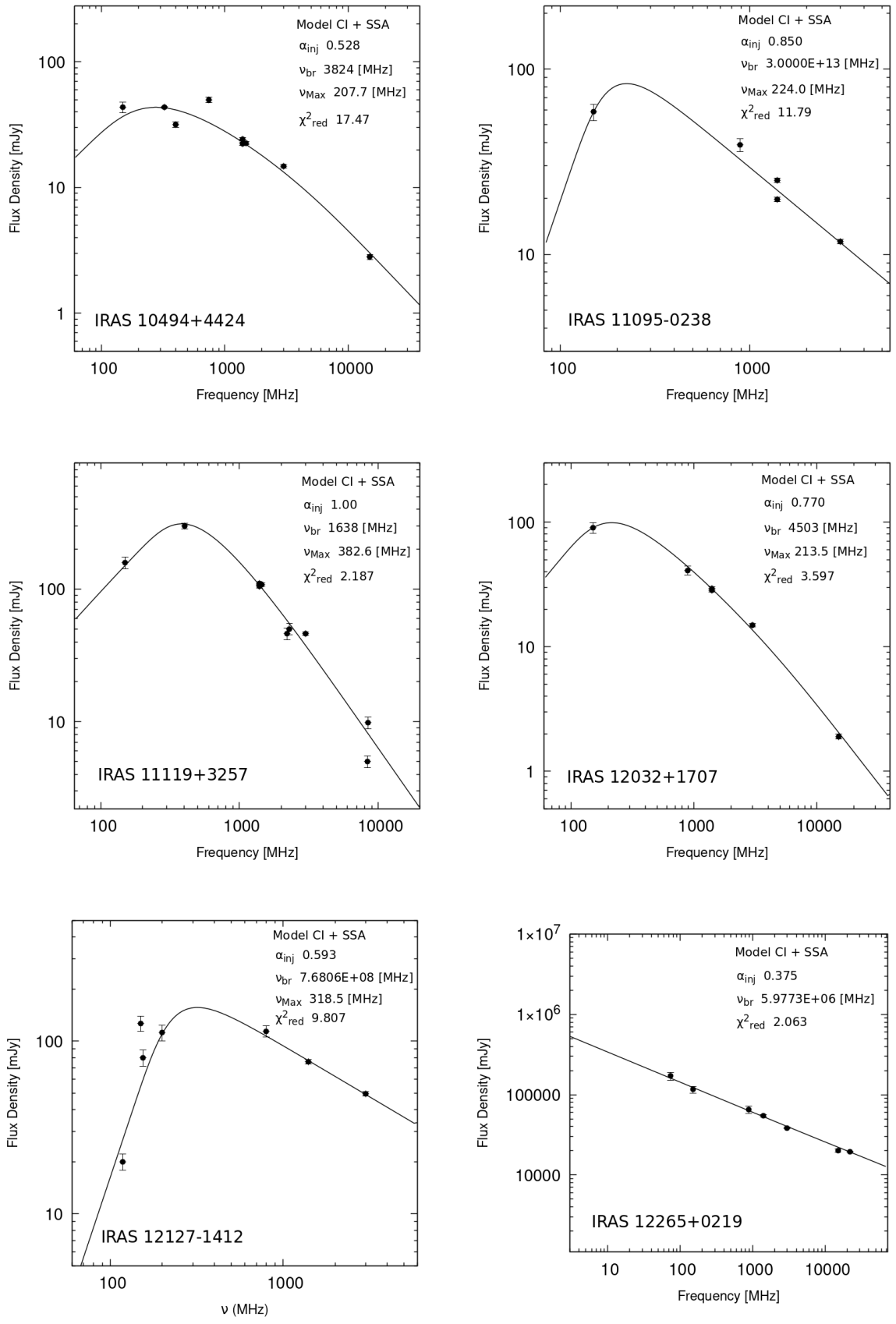

Figure 5. Radio spectra modelled using SYNAGE. Panels show the SEDs for IRAS 10494+4424, IRAS 11095−0238, IRAS 11119+3257, IRAS 12032+1707, IRAS 12127−1412, and IRAS 12265+0219.

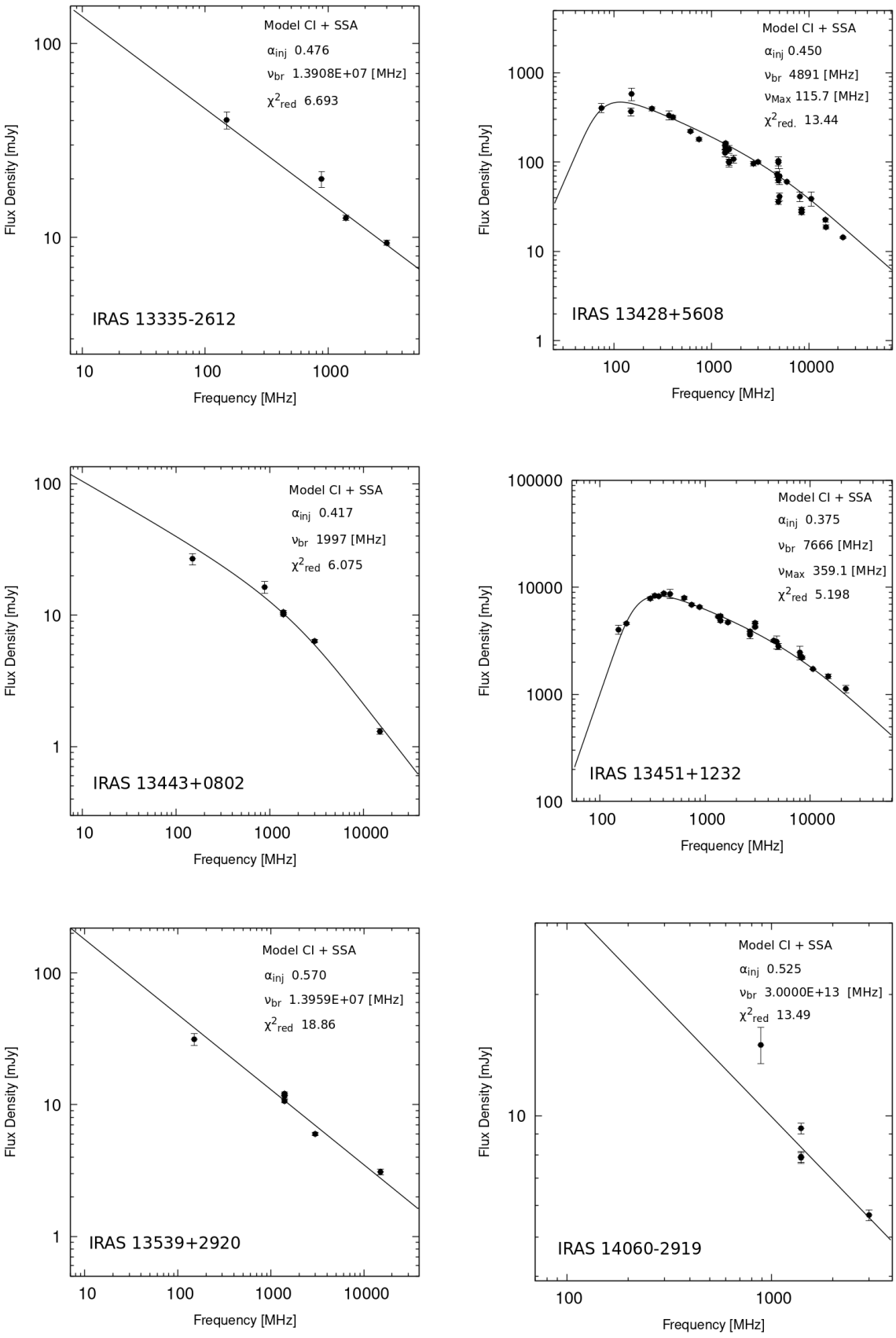

Figure 6. Radio spectra modelled using SYNAGE. Panels show the SEDs for IRAS 13335−2612, IRAS 13428+5608, IRAS 13443+0802, IRAS 13451+1232, IRAS 13539+2920, and IRAS 14060−2919.

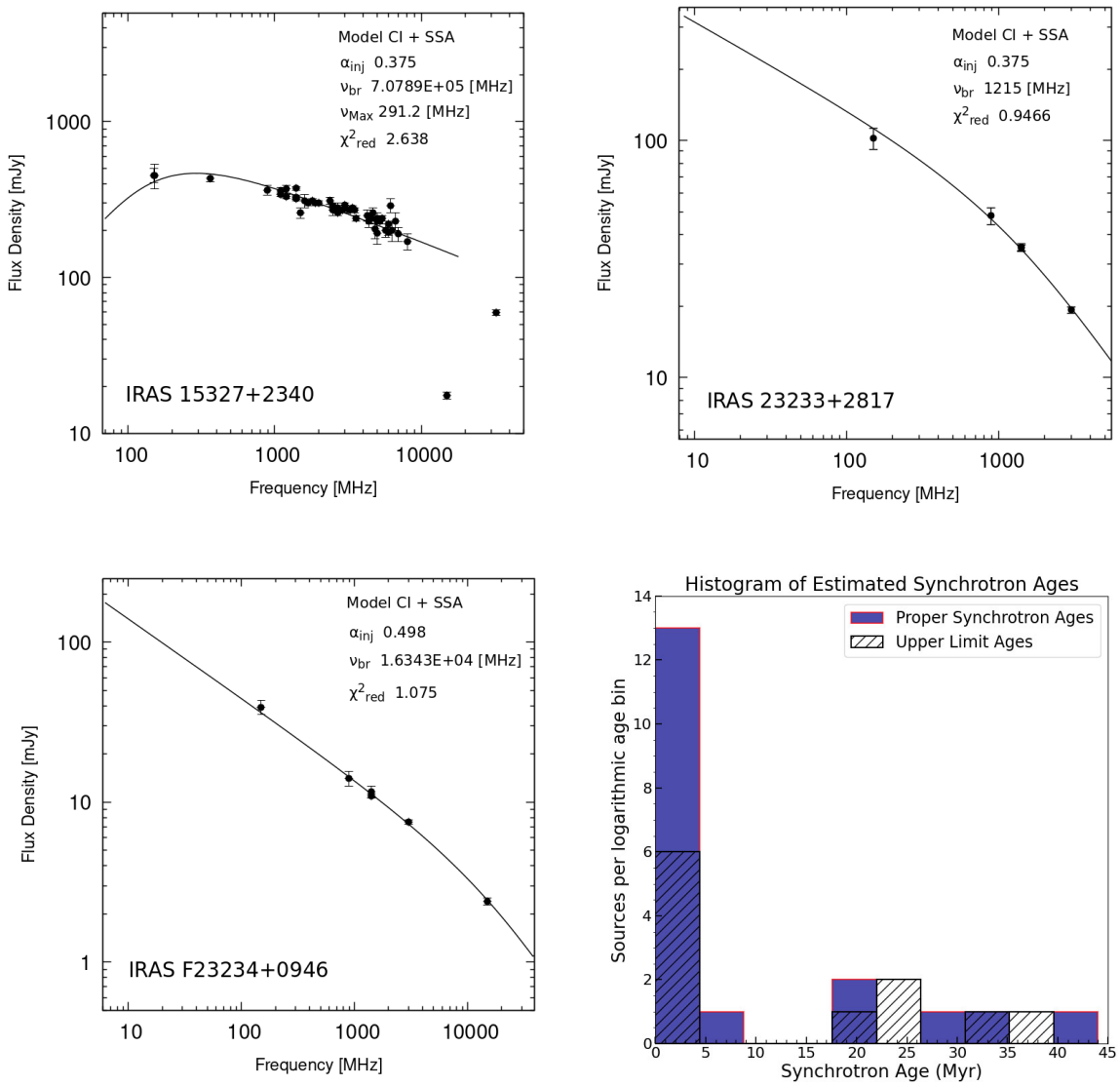

Figure 7. Radio spectra modelled using SYNAGE. Panels show the SEDs for IRAS 15327+2340, IRAS 23233+2817, IRAS F23234 + 0946, and distribution of synchrotron ages for the radio sources. Filled bars show proper age estimates; and hatched bars indicate upper limits.

red denotes $W1 - W2 > 0.8$, generally associated with AGN-dominated systems. The blue vertical line represents the median synchrotron age (0.76 Myr) for sources with $W1 - W2 \leq 0.8$, and the red vertical line marks the median age (1.40 Myr) for sources with $W1 - W2 > 0.8$. Binary detected sources for which spectral ages have been estimated are further highlighted using concentric circles: IRAS 13443+0802 (lime green), IRAS 13451+1232 (yellow), and IRAS F23234 + 0946 (cyan). According to S. Veilleux et al. (2002) and J. Rodríguez Zaurín, C. N. Tadhunter & R. M. González Delgado (2009), our sample includes 12 pre-merger sources, 18 merger-stage sources, and 4 post-merger sources, classified based on optical wavelength observations. The interaction classification for each source is provided in Table 6. In this second panel, sources with $W1 - W2 \leq 0.8$ suggest a possible AGN presence, typically associated with the pre-merger phase. Whereas sources with $W1 - W2 > 0.8$ indicate confirmed AGN activity, corresponding to the merger and post-merger phases. Most of the sources in our sample are in the merger stage and have $W1 - W2 > 0.8$. The majority of sources in this plot with $W1 - W2 > 0.8$ have lower synchrotron ages, suggesting a connection between the *WISE* colour, the merger stage identified in optical observations, and radio synchrotron aging.

The third panel displays a bar plot showing the distribution of optical interaction classes, based on the classification scheme from S. Veilleux et al. (2002), expressed as a percentage of the total sample. Most of the sources in our sample are in the merger stage and exhibit $W1 - W2 > 0.8$. The majority of these sources also exhibit relatively lower synchrotron ages, suggesting a possible connection between the *WISE* colour, the merger stage (as identified through optical observations), and radio synchrotron aging. Specifically, the median synchrotron age for sources with $W1 - W2 > 0.8$ (red points), which tend to be in the merger or post-merger stages, is 1.46 Myr, indicating older

Table 5. Radio and IR flux densities, logarithmic luminosities, and FIR-to-radio ratios (q_ν) for the ULIRGs in the sample.

Galaxy	$S_{1.4\mathrm{GHz}}$ (10^{-28} W m^{-2} Hz^{-1})	$\log L_{1.4\mathrm{GHz}}$ (W Hz^{-1})	$S_{60\mu\mathrm{m}}$ (Jy)	$\mathrm{Err}_{S_{60\mu\mathrm{m}}}$ (Jy)	$\log L_{60\mu\mathrm{m}}$ ($L_\odot$)	$S_{100\mu\mathrm{m}}$ (Jy)	$\mathrm{Err}_{S_{100\mu\mathrm{m}}}$ (Jy)	FIR	q_ν
(1)	(2)	(3)	(4)	(5)	(6)	(7)	(8)	(9)	(10)
IRAS 00188−0856♦	1.65 ± 0.05	23.844	2.592E + 00	2.33E − 01	11.974	3.403E + 00	3.40E − 01	1.27E − 13	2.313
IRAS 00456−2904	2.14 ± 0.06	23.806	2.598E + 00	1.82E − 01	11.825	3.377E + 00	3.71E − 01	1.27E − 13	2.199
IRAS F01004−2237†	1.37 ± 0.06	23.678	2.287E + 00	1.60E − 01	11.835	1.790E + 00	1.79E − 01	9.69E − 14	2.276
IRAS 01494−1845†	0.80 ± 0.02	23.729	1.288E + 00	9.02E − 02	11.871	1.846E + 00	2.58E − 01	6.51E − 14	2.337
IRAS 01569−2939	12.39 ± 0.37	24.797	1.734E + 00	1.39E − 01	11.878	1.514E + 00	1.82E − 01	7.54E − 14	1.211
IRAS 01572 + 0009♦	2.70 ± 0.09	24.236	2.224E + 00	1.78E − 01	12.138	2.164E + 00	2.81E − 01	9.96E − 14	1.993
IRAS 02480−3745†	1.31 ± 0.03	23.985	1.252E + 00	6.26E − 02	11.900	1.487E + 00	1.34E − 01	5.94E − 14	2.519
IRAS 04103−2838†	1.37 ± 0.02	23.678	1.823E + 00	9.12E − 02	11.737	1.707E + 00	1.71E − 01	8.08E − 14	2.196
IRAS 05156−3024	1.87 ± 0.05	24.174	1.162E + 00	6.97E − 02	11.902	1.402E + 00	1.68E − 01	5.54E − 14	1.898
IRAS 05189−2524	2.91 ± 0.08	23.111	1.367E + 01	5.47E − 01	11.717	1.136E + 01	5.68E − 01	5.88E − 13	2.731
IRAS F07599 + 6508	4.17 ± 0.12	24.384	1.692E + 00	8.46E − 02	11.927	1.730E + 00	1.90E − 01	7.68E − 14	1.691
IRAS 08559 + 1053	1.22 ± 0.03	23.850	1.119E + 00	6.71E − 02	11.747	1.952E + 00	2.54E − 01	6.10E − 14	2.125
IRAS 10494 + 4424	2.24 ± 0.08	23.668	3.527E + 00	2.12E − 01	11.800	5.412E + 00	3.25E − 01	1.83E − 13	2.338
IRAS 11095−0238	2.51 ± 0.07	23.849	3.249E + 00	1.62E − 01	11.896	2.531E + 00	2.53E − 01	1.37E − 13	2.165
IRAS 11119 + 3257	11.00 ± 0.33	25.030	1.588E + 00	1.75E − 01	12.124	1.523E + 00	1.68E − 01	7.08E − 14	1.235
IRAS 12032 + 1707	2.84 ± 0.08	24.587	1.358E + 00	9.51E − 02	12.201	1.543E + 00	1.85E − 01	6.36E − 14	1.776
IRAS 12112 + 0305♦	2.40 ± 0.12	23.537	8.503E + 00	5.10E − 01	11.969	9.976E + 00	7.98E − 01	4.02E − 13	2.650
IRAS 12127−1412	7.60 ± 0.22	24.543	1.538E + 00	9.23E − 02	11.784	1.134E + 00	1.81E − 01	6.43E − 14	1.353
IRAS 12265 + 0219	5499.2 ± 110.95	27.699	2.060E + 00	1.44E − 01	12.075	2.891E + 00	2.02E − 01	1.03E − 13	−1.300
IRAS 13305−1739♦	4.83 ± 0.15	24.445	1.164E + 00	9.31E − 02	11.764	1.044E + 00	2.51E − 01	5.09E − 14	1.450
IRAS 13335−2612	1.26 ± 0.03	23.704	1.402E + 00	1.12E − 01	11.685	2.101E + 00	2.10E − 01	7.20E − 14	2.183
IRAS 13428 + 5608	14.5 ± 0.52	23.662	2.174E + 01	8.70E − 01	11.771	2.138E + 01	8.55E − 01	9.76E − 13	2.253
IRAS 13443 + 0802	1.05 ± 0.03	23.691	1.300E + 00	1.43E − 01	11.718	1.940E + 00	1.74E − 01	6.67E − 14	2.229
IRAS 13451 + 1232	539.70 ± 16.19	26.305	1.916E + 00	2.11E − 01	11.790	2.060E + 00	1.85E − 01	8.82E − 14	−0.361
IRAS 13539 + 2920	1.21 ± 0.03	23.550	1.830E + 00	1.28E − 01	11.664	2.730E + 00	1.91E − 01	9.39E − 14	2.316
IRAS 14060 + 2919	0.93 ± 0.02	23.502	1.611E + 00	1.61E − 01	11.675	2.417E + 00	1.69E − 01	8.28E − 14	2.376
IRAS 14070 + 0525♦	0.50 ± 0.02	24.023	1.447E + 00	8.68E − 02	12.422	1.821E + 00	1.64E − 01	7.00E − 14	2.572
IRAS 14394 + 5332♦	4.20 ± 0.21	24.064	1.954E + 00	7.82E − 02	11.666	2.395E + 00	1.20E − 01	9.37E − 14	1.774
IRAS 15001 + 1433♦	1.70 ± 0.01	24.080	1.871E + 00	9.36E − 02	12.057	2.043E + 00	1.84E − 01	8.66E − 14	2.133
IRAS 15327 + 2340	32.60 ± 0.97	23.367	1.038E + 02	4.15E + 00	11.804	1.124E + 02	3.37E + 00	4.79E − 12	2.593
IRAS 16156 + 0146♦	0.83 ± 0.04	23.574	1.126E + 00	6.76E − 02	11.641	1.003E + 00	2.21E − 01	4.92E − 14	2.199
IRAS 17028 + 5817♦	1.50 ± 0.01	23.625	2.430E + 00	1.46E − 01	11.769	3.910E + 00	1.96E − 01	1.28E − 13	2.358
IRAS 17044 + 6720♦	0.50 ± 0.02	23.382	1.281E + 00	6.41E − 02	11.725	0.978E + 00	1.57E − 01	5.40E − 14	2.459
IRAS 17179 + 5444♦	33.60 ± 1.70	25.284	1.362E + 00	6.81E − 02	11.826	1.915E + 00	1.53E − 01	6.84E − 14	0.735
IRAS 23060 + 0505♦	0.65 ± 0.03	23.720	1.152E + 00	8.06E − 02	11.904	8.329E − 01	1.75E − 01	4.79E − 14	2.294
IRAS 23233 + 2817	3.55 ± 0.12	24.059	1.262E + 00	1.26E − 01	11.545	2.107E + 00	3.37E − 01	6.76E − 14	1.706
IRAS F23234 + 0946	1.16 ± 0.01	23.691	1.561E + 00	9.37E − 02	12.754	2.108E + 00	2.95E − 01	7.73E − 14	2.250
IRAS 23389 + 0300♦	86.30 ± 2.60	25.680	1.233E + 00	1.48E − 01	11.770	1.171E + 00	2.58E − 01	5.48E − 14	0.229

Notes. The table presents derived radio and IR flux densities, logarithmic luminosities, and FIR-to-radio ratios (q_ν) for the ULIRG sample. The columns are as follows: (1) source name: sources names marked with (♦): 13 sources were extracted from S. Nandi et al. (2021); sources marked with (†) have their spectral indices estimated using two different methods: three sources were fitted with a power-law model using GNUPLOT, while one source had its two-point spectral index calculated; (2) radio flux of the object at 1.4 GHz in units of 10^{-28} W m^{-2} Hz^{-1} (J. J. Condon et al. 1998); (3) logarithmic radio luminosity at 1.4 GHz in units of W Hz^{-1}; (4) flux at 60 μm (M. Moshir et al. 1990); (5) error in flux at 60 μm (M. Moshir et al. 1990); (6) logarithmic luminosity at 60 μm in units of $L_\odot$; (7) flux at 100 μm (M. Moshir et al. 1990); (8) error in flux at 100 μm (M. Moshir et al. 1990); (9) FIR-to-radio ratio (M. S. Yun et al. 2001); and (10) 'q_ν' factor at 1.4 GHz calculated as suggested in M. S. Yun et al. (2001).

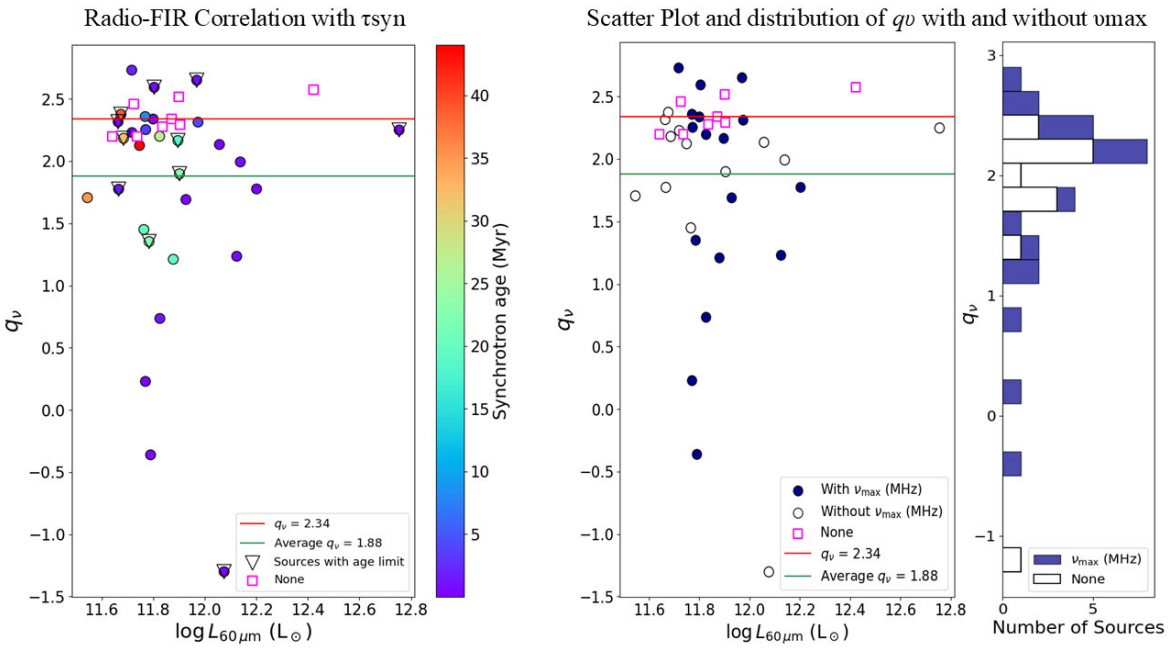

Figure 8. The figure illustrates the relationship between q_ν and $\log L_{60\,\mu m}$ in the first panel based on synchrotron age, where scatter points are colour-coded by radio synchrotron age, and in the second panel based on turnover frequency, where scatter points are classified according to turnover frequency. The third panel shows a histogram of turnover classifications based on the second panel. The green line in first and second panels represents the average q_ν value for the entire sample, while the red line marks the threshold at $q_\nu = 2.34$. According to M. S. Yun et al. (2001), sources below this threshold are classified as radio excess, while those above are IR excess. In the second panel, filled circles indicate sources with turnover frequency, open circles represent sources without a turnover frequency. Squares in the first and second panels denote sources for which spectral age could not be determined due to insufficient data.

radio-emitting plasma. In comparison, sources with $W1 - W2 \leq 0.8$ (blue points), typically associated with the pre-merger stage, have a median age of 0.73 Myr, reflecting younger synchrotron plasma. This trend suggests a potential relationship between MIR colour, galaxy interaction stage, and the synchrotron age.

Although our sample size is small, the observed trend suggests a possible link between synchrotron age, *WISE* MIR colour, and the galaxy's merger stage. We expect that with a larger sample, this relationship will become clearer and more statistically significant.

5 DISCUSSION

5.1 GPS/CSS characteristics

GPS and CSS sources are typically associated with young radio galaxies, characterized by a peaked radio spectrum (C. Fanti et al. 1995; C. P. O'Dea 1998; J. D. Collier et al. 2018; C. P. O'Dea & D. J. Saikia 2020). Above the peak, the spectrum steepens in the optically thin region. In this study, we analyse the integrated radio spectrum of a large sample of ULIRGs. Table 4 presents SYNAGE output parameters, including magnetic field and spectral age, for 38 sources [13 sources from previous work highlighted with (♦), and 25 sources from this work]. According to our findings, the integrated radio spectra of 17 ULIRGs from our total sample show low-frequency turnover ranging from 63 to 509 MHz, with spectral age spanning from 0.0093 to 44 Myr. The variation of q_ν values spectral age and turnover frequency for the whole sample is shown in Fig. 8. In this sample, eight sources indicate a very young spectral age, with estimated ages < 1 Myr. We note very high break frequency for 11 sources. We consider their break frequency must be higher than the highest available frequency used for SYNAGE fitting. For these 11 sources, we estimate only an upper age limit. In our sample, the majority of sources appear compact, with unresolved radio structures. From available high-frequency data, we find that eight sources have resolved radio structure. For most ULIRGs, the highest available angular resolution data are provided by VLASS at 3 GHz, and the redshift range of the sample is from 0.034 to 0.264. Since the VLASS resolution is 2.5 arcsec, we cannot resolve the nearest source of the sample with linear size $\lesssim$1 kpc. Similarly the most distant source with linear size $\lesssim$4 kpc can not be resolved by VLASS. Unavailability of resolved images limits reliable measurements of projected linear sizes. As a result, GPS/CSS classification is not possible for many sources from their linear size criteria. However, depending on the turn over frequency range below 400 MHz (except the source IRAS 17179+5444 which shows turnover at 509 MHz) and spectral age, our sample shows young CSS characteristics. Few sources may also appear as double nucleus system. The optical-radio contour overlays in Fig. B1 highlight the most five interesting sources within our sample. High-frequency radio data are necessary to confirm their GPS/CSS nature. The presence of several young compact GPS/CSS radio sources in a relatively large sample of ULIRG strongly suggests that they represent radio galaxies in early stages of evolution.

5.2 Buried AGN

Buried AGNs are active galactic nuclei whose central regions are heavily obscured by surrounding dust and gas (M. Imanishi, R. Maiolino & T. Nakagawa 2010). Although the black hole is actively accreting and emitting energy, the radiation output,

Table 6. Nuclear structures, separations, interaction classes, and *WISE* magnitudes of ULIRGs in the sample.

Galaxy	Nuclear structure	NS (Opt) (arcsec)	NS (IR) (arcsec)	NS (RF) (arcsec)	Interaction class	$W1$ (mag)	$W2$ (mag)	$W1-W2$ (mag)
(1)	(2)	(3)	(4)	(5)	(6)	(7)	(8)	(9)
IRAS 00188−0856♦	S(Opt), S(IR), S(RF)				Post-merger	12.318	10.442	1.876
IRAS 00456−2904	D(Opt), S(IR), S(RF)	8.327			Pre-merger	12.725	12.048	0.677
IRAS F01004−2237 †	S(Opt), S(IR), S(RF)				Post-merger	12.887	11.256	1.631
IRAS 01494−1845†	S(Opt), S(IR), S(RF)				Merger	13.401	12.470	0.931
IRAS 01569−2939	S(Opt), S(IR), S(RF)				Merger	13.877	12.942	0.935
IRAS 01572 + 0009♦	S(Opt), S(IR), T(RF)			0.340	Merger	10.790	9.792	0.998
IRAS 02480−3745†	S(Opt), S(IR), S(RF)				Merger	14.580	13.736	0.844
IRAS 04103−2838†	S(Opt), S(IR), S(RF)				Merger	12.321	11.035	1.286
IRAS 05156−3024	S(Opt), S(IR), S(RF)				Merger	13.497	12.506	0.991
IRAS 05189−2524	S(Opt), S(IR), D(RF)			1.042	Merger	8.649	7.524	1.125
IRAS F07599 + 6508	S(Opt), S(RF)				Merger			
IRAS 08559 + 1053	S(Opt), S(IR), S(RF)				Merger	11.551	10.490	1.061
IRAS 10494 + 4424	S(Opt), S(IR), S(RF)				Merger	12.766	11.909	0.857
IRAS 11095−0238	S(Opt), S(IR), S(RF)				Merger	13.679	11.959	1.720
IRAS 11119 + 3257	S(Opt), S(IR), S(RF)				Merger	9.906	8.845	1.061
IRAS 12032 + 1707	D(Opt), S(IR), S(RF)	2.278			Pre-merger	14.065	13.105	0.960
IRAS 12112 + 0305♦	D(Opt), S(IR), D(RF)	2.484		2.721	Pre-merger	12.257	11.455	0.802
IRAS 12127−1412	D(Opt), S(IR), S(RF)	7.170			Pre-merger	10.891	9.338	1.553
IRAS 12265 + 0219	S(Opt), S(IR), S(RF)				Merger	8.395	7.425	0.970
IRAS 13305−1739♦	S(Opt), S(IR), E(RF)				Post-merger	12.626	11.061	1.565
IRAS 13335−2612	D(Opt), S(IR), S(RF)	1.120			Pre-merger	12.942	12.374	0.568
IRAS 13428 + 5608	D(Opt), S(IR), E(RF)	0.880		1.243	Merger	10.416	9.234	1.182
IRAS 13443 + 0802	T(Opt), D(IR), D(RF)	5.741	5.544	7.552	Triple	12.73, 13.85	12.16, 12.56	0.57, 1.29
IRAS 13451 + 1232	D(Opt), D(IR), D(RF)	1.509	4.896	2.000	Pre-merger	11.52, 13.42	10.21, 12.72	1.31, 0.7
IRAS 13539 + 2920	D(Opt), S(IR), D(RF)	3.033			Pre-merger	12.861	12.064	0.797
IRAS 14060 + 2919	S(Opt), S(IR), S(RF)				Merger	12.744	12.003	0.741
IRAS 14070 + 0525♦	S(Opt), S(IR), S(RF)				Post-merger	14.244	13.287	0.957
IRAS 14394 + 5332♦	T(Opt), S(IR), S(RF)				Triple	12.384	10.963	1.421
IRAS 15001 + 1433♦	T(Opt), S(IR), E(RF)				Triple	12.337	11.049	1.288
IRAS 15327 + 2340	D(Opt), S(IR), D(RF)	1.049		2.462	Pre-merger	10.079	9.327	0.752
IRAS 16155 + 0146♦	D(Opt), S(IR), S(RF)	2.475			Pre-merger	13.105	10.715	2.39
IRAS 17028 + 5817♦	D(Opt), S(IR), S(RF)	10.288			Pre-merger	13.401	12.321	0.783
IRAS 17044 + 6720♦	S(Opt), D(IR), S(RF)		11.268		Merger	11.97, 14.96	10.44, 14.86	1.53, 0.1
IRAS 17179 + 5444♦	S(Opt), S(IR), S(RF)				Merger	12.724	11.506	1.218
IRAS 23060 + 0505♦	S(Opt), S(IR), S(RF)				Merger	9.809	8.614	1.195
IRAS 23233 + 2817	S(Opt), S(IR), S(RF)				Iso	12.512	11.241	1.271
IRAS F23234 + 0946	D(Opt), D(IR), S(RF)	2.661	5.004		Pre-merger	13.66, 14.73	12.69, 14.43	0.97, 0.3
IRAS 23389 + 0300♦	D(Opt), S(IR), D(RF)	1.460		0.208	Pre-merger	13.698	12.694	1.004

Notes. The table presents the sources in our sample along with their nuclear structures, NSs in arcseconds, interaction classifications, and *WISE* magnitudes. The columns are as follows: (1) source name: sources names marked with (♦): 13 sources were extracted from S. Nandi et al. (2021); sources marked with (†) have their spectral indices estimated using two different methods: three sources were fitted with a power-law model using GNUPLOT; (2) nuclear structure in the optical (Opt), infrared (IR), and radio frequency (RF) bands, where S = single, D = double, T = triple ,and E = extended; (3), (4), and (5) NS between two nuclei measured in the optical, IR, and radio bands, respectively, in arcseconds; (6) interaction classes are based on optical morphological features, as classified by S. Veilleux et al. (2002); (7) and (8) *WISE* magnitudes, and (9) calculated *WISE* colour ($W1-W2$) in magnitudes (L. Blecha et al. 2018).

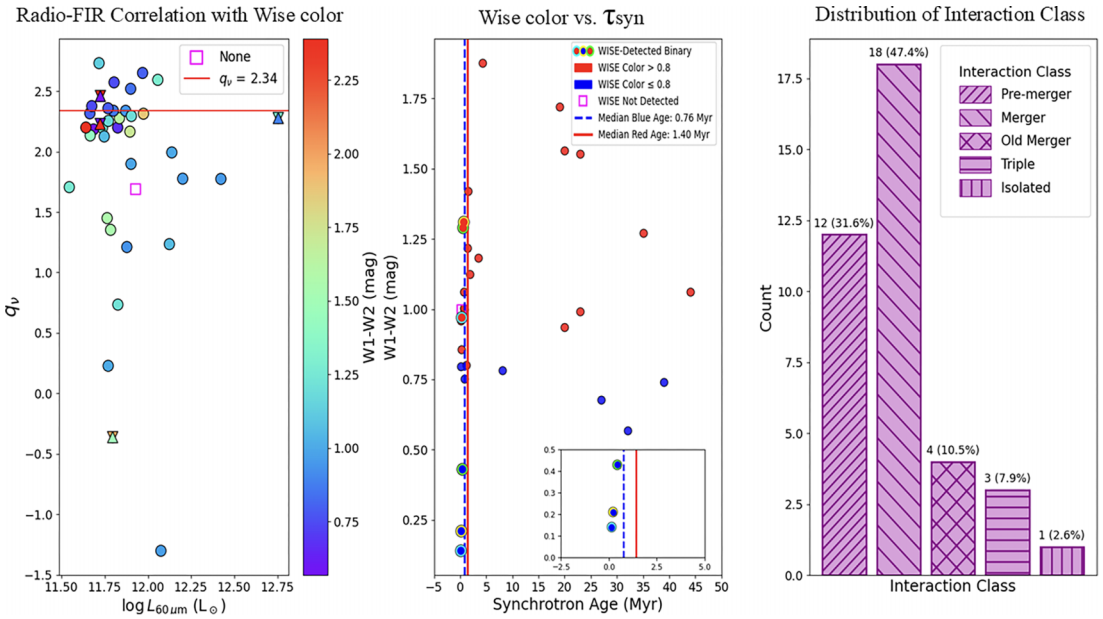

Figure 9. The first panel shows a scatter plot of q_ν versus $\log L_{60\mu m}$, with points classified based on the *WISE* colour cut criteria ($W1-W2$) for AGN detection, as defined by L. Blecha et al. (2018). Upward and downward triangles indicate sources detected as binaries in the *WISE* catalogue, located at the same RA and Dec. coordinates but exhibiting different *WISE* magnitudes. A square indicates the source not detected in the *WISE* catalogue. The red horizontal line marks the average q_ν value of 2.34 (M. S. Yun et al. 2001). The second panel presents a scatter plot of *WISE* colour-cut ($W1-W2$) values against synchrotron age. The *WISE* colour cut categorizes sources as follows: values ≤ 0.8 correspond to star formation or a possible AGN presence, while values > 0.8 confirm AGN activity, typically associated with the merger or post-merger phase. Binary-detected sources with two different *WISE* colour values are represented by overlaid concentric circles, each outlined in a distinct colour. The blue and red vertical lines mark the median synchrotron ages of sources with $W1-W2 \leq 0.8$ (0.76 Myr) and $W1-W2 > 0.8$ (1.40 Myr), respectively. An inset within this panel shows a zoomed view of the synchrotron age range −2.5 to 5 Myr, highlighting the separation between the median age distributions. The third panel displays a bar plot showing the distribution of interaction classes, based on optical classification (S. Veilleux et al. 2002), expressed as a percentage of the total sample.

particularly in optical and X-ray wavelengths, is often obscured, making direct detection challenging. In the previous section, we noted that six sources IRAS 00188−0856, IRAS 05189−2524, IRAS 10494+4424, IRAS 12112+0305, IRAS 15327+2340, and IRAS 17028 + 5817 exhibit q_ν values greater than 2.34, suggesting that their far-IR emission is likely dominated by starburst activity. Interestingly, when we modelled their radio SEDs (Figs 4, 5, 6, and 7), we found that the radio emission in these sources is primarily non-thermal, with clear low-frequency turnovers and young spectral ages. These are key features of compact, young radio AGNs. The combination of starburst dominated far-IR emission and signs of AGN activity in the radio suggests that these galaxies may host young AGNs still embedded within dusty, star forming environments. Fig. 8 highlights these findings. In the left panel, these six sources lie above the $q_\nu = 2.34$ threshold (left panel), suggesting starburst dominance, while appearing in blue in the age colour map, indicating their youth. In the right panel (Fig. 8), all six sources show detectable turnover frequencies, supporting their classification as young radio AGNs. The corresponding spectral ages and turnover frequencies are listed in Table 4, while FIR fluxes and q_ν values are provided in Table 5.

The presence of excess radio emission, even in systems with high q_ν values, highlights the obscured nature of these AGNs. While they are not easily identified in the IR alone, the shape of their radio spectra reveals the activity of the central engine.

Additional evidence from other wavelengths supports the interpretation of these sources as buried AGNs. According to the optical nuclear classifications from S. Veilleux et al. (2002), IRAS 05189−2524 is classified as a Seyfert 2 galaxy, while the other five sources are classified as LINERs. Both types are typically associated with obscured AGN activity. All six sources also have *WISE* $W1-W2$ colour values greater than 0.5: IRAS 00188−0856 (1.876), IRAS 05189−2524 (1.125), IRAS 10494+4424 (0.857), IRAS 12112+0305 (0.802), IRAS 15327+2340 (0.752), and IRAS 17028 + 5817 (0.783) satisfying common MIR AGN-selection criteria (D. Stern et al. 2012; R. J. Assef et al. 2013; L. Blecha et al. 2018). This suggests that, although some AGN signatures can be detected in the optical or MIR, the central engines in these galaxies are largely hidden and are best revealed through their compact radio emission. In a recent study T. J. Hayashi et al. (2025) confirmed IRAS 00188−0856 as a buried AGN using Very Long Baseline Array observations.

5.3 Interaction class characteristics and *WISE*–radio trends

In our sample, 31.6 per cent of ULIRGs are classified as pre-merger systems, 47.4 per cent as mergers, and 10.5 per cent as post-mergers. We compared the interaction classes defined by S. Veilleux et al. (2002) with the estimated *WISE* colour $W1-W2$ to constrain different phases of galaxy evolution. As shown in Table 6, we observe a correlation between the interaction class and *WISE* colour $W1-W2$ values in our sample. There is a significant trend between radio excess and $W1-W2$ colour, as illustrated in Fig. 9 (first panel), where redder objects tend to exhibit higher radio excess though a few exceptions exist. We also found a tendency for higher synchrotron age for colour >0.8. As the *WISE* colour goes blue to red, both the radio excess, and spectral age vary from low to high. A general trend is post-merger

interaction has higher *WISE* colour. We also note the nuclear structure and its component separations in optical, IR, and radio wavelengths for these interaction systems. This multiwavelength comparison indicates that the systems are about to merge or have already merged (see in Table 6).

In Table 6, we provide details on the interaction classification, including nuclear structure and nuclear separation (NS) across optical, IR, radio wavelengths, and *WISE* magnitudes. The source IRAS 13443 + 0802, appears as a triple system in optical (Fig. B1), but is observed as a double system in both radio and IR. Its estimated $W1 - W2$ values are 0.57 and 1.29 (mag). Based on the *WISE* colour, one component of this system is classified as an AGN, while the other exhibits characteristics of starburst activity. Similarly, IRAS 13451 + 1232 is identified as a double system across optical, radio, and IR wavelengths. The estimated $W1-W2$ values for its components are 1.31 and 0.7, both consistent with AGN activity. The source IRAS 17044 + 6720, classified as a single system in optical according to S. Veilleux et al. (2002), is detected as a double system in the IR. Its estimated $W1 - W2$ values are 1.53 and 0.1, indicating starburst and AGN activity, respectively. The $W1 - W2$ values for all sources are depend on their interaction class. Most of the sources in our sample are merger systems.

6 CONCLUSIONS

In this study, we have investigated different statistical properties of a large sample of ULIRGs. Multifrequency radio data of ULIRGs provides a better quantitative understanding of their radio spectrum, spectral indices, spectral age, and morphology. We performed a non-linearity test of radio–FIR correlation, estimated the *WISE* colour, compared the interaction class, and checked the evolution process from ULIRG to young radio source.

The spectral shape mostly follows a power law with a high-frequency spectral break and low-frequency concave turnover between 63 to 509 MHz. It was possible to estimate the spectral age for 30 sources using archival data and new observations. The spectral age of 19 sources is <5 Myr and 17 sources show a low-frequency turnover. There are three extended structures, eight resolved double nuclei, and one triple component in radio. 14 sources show the double nuclear structure and 3 triple nuclear structures in the optical wave band (based on the information from S. Veilleux et al. 2002).

Four sources show double components in the *WISE* catalogue. The extended or resolved radio structures that are associated with a single optical or IR nuclear component, may evolve into a CSS sources. Whereas a single component in radio hosting more than a single nuclear component in optical/IR may have binary AGN. Double components in all three bands strongly indicate the possibility of binary AGN. We plan to perform high-frequency radio observations of these ULIRGs in the future.

Most of the ULIRGs in our sample show a dispersion in the radio–FIR correlation and exhibit a radio excess of AGN origin. Radio excess and spectral age have a strong correlation with *WISE* colour. ULIRGs with higher spectral ages and higher redder colours may follow the 'frustration scenario' while the major population of our sample follow the 'youth hypothesis' and they may evolve into GPS/CSS sources. We also note that six sources with a starburst origin have low-frequency turnovers. These ULIRGs may host buried AGNs.

ACKNOWLEDGEMENTS

The authors gratefully acknowledge the anonymous referee for the thoughtful and constructive feedback, which has greatly contributed to improving this manuscript. SN acknowledges support by the Anusandhan National Research Foundation (ANRF) as well as the Science and Engineering Research Board (SERB), a statutory body of Department of Science and Technology (DST), Government of India (Scheme: State University Research Excellence (SERB SURE); file no.: SUR/2022/003864). We thank the GMRT staff for technical support during the observations. GMRT is run by the National Centre for Radio Astrophysics of the Tata Institute of Fundamental Research. This research has also made use of the NASA/IPAC Extragalactic Database (NED), which is operated by the Jet Propulsion Laboratory, California Institute of Technology, under contract with the National Aeronautics and Space Administration (NASA). MD acknowledges the support of the Science and Engineering Research Board (SERB) core research grant (CRG/2022/004531) and the Department of Science and Technology (DST) grant (DST/WIDUSHIA/PM/2023/25(G)) for this research.

DATA AVAILABILITY

The data underlying this article can be shared on reasonable request to the corresponding author. The GMRT raw data can be obtained from the following link: https://naps.ncra.tifr.res.in/goa/data/search.

REFERENCES

Adgie R. L., Crowther J. H., Gent H., 1972, MNRAS, 159, 233
Allison J., Sadler E., Meekin A., 2014, MNRAS, 440, 696
Assef R. J. et al., 2013, ApJ, 772, 26
Bach U. et al., 2007, A&A, 464, 175
Basu A., Roy S., Mitra D., 2012, ApJ, 756, 141
Bean B. et al., 2022, PASP, 134, 114501
Becker R. H., White R. L., Edwards A. L., 1991, ApJS, 75, 1
Becker R. H., White R. L., Helfand D. J., 1995, ApJ, 450, 559
Bicay M. D., Kojoian G., Seal J., Dickinson D. F., Malkan M. A., 1995, ApJS, 98, 369
Blecha L., Snyder G. F., Satyapal S., Ellison S. L., 2018, MNRAS, 478, 3056
Bourda G., Charlot P., Porcas R. W., Garrington S. T., 2010, A&A, 520, A113
Brown M. J. I. et al., 2017, ApJ, 847, 136
Bushouse H. A. et al., 2002, ApJS, 138, 1
Calderón-Castillo P., Smith R., 2024, A&A, 691, A82
Carilli C. L., Taylor G. B., 2000, ApJ, 532, L95
Cicone C. et al., 2018, ApJ, 863, 143
Clemens M. S., Vega O., Bressan A., Granato G. L., Silva L., Panuzzo P., 2008, A&A, 477, 95
Clemens M. S., Scaife A., Vega O., Bressan A., 2010, MNRAS, 405, 887
Clements D. L., Sutherland W. J., McMahon R. G., Saunders W., 1996, MNRAS, 279, 477
Collier J. D. et al., 2018, MNRAS, 477, 578
Condon J., Condon M. A., Broderick J., Davis M., 1983, AJ, 88, 20
Condon J. J., Helou G., Sanders D. B., Soifer B. T., 1990, ApJS, 73, 359
Condon J. J., Anderson M. L., Helou G., 1991, ApJ, 376, 95
Condon J. J., Cotton W. D., Greisen E. W., Yin Q. F., Perley R. A., Taylor G. B., Broderick J. J., 1998, AJ, 115, 1693
Dasyra K. et al., 2006, ApJ, 638, 745
Douglas J. N., Bash F. N., Bozyan F. A., Torrence G. W., Wolfe C., 1996, AJ, 111, 1945
Dressel L., Condon J., 1978, ApJS, 36, 53
Duc P.-A., Mirabel I., Maza J., 1997, A&AS, 124, 533

Evans A. S., Kim D. C., Mazzarella J. M., Scoville N. Z., Sanders D. B., 1999, ApJ, 521, L107
Fanti C., Fanti R., Dallacasa D., Schilizzi R. T., Spencer R. E., Stanghellini C., 1995, A&A, 302, 317
Ficarra A., Grueff G., Tomasi P., Righini R., 1990, A&AS, 82, 339
Gear W. K. et al., 1994, MNRAS, 267, 167
Gordon Y. A. et al., 2021, ApJS, 255, 30
Gower J. F. R., Scott P. F., Wills D., 1967, Mem. RAS, 71, 49
Gregory P. C., Condon J. J., 1991, ApJS, 75, 1011
Gregory P. C., Scott W. K., Douglas K., Condon J. J., 1996, ApJS, 103, 427
Greisen E. W., 2003, in Heck A., ed., Astrophysics and Space Science Library, Vol. 285, Information Handling in Astronomy – Historical Vistas. Springer, Dordrecht, p. 109
Gupta Y. et al., 2017, Curr. Sci., 113, 707
Hale C. L. et al., 2021, Publ. Astron. Soc. Aust., 38, e058
Hales S. E. G., Masson C. R., Warner P. J., Baldwin J. E., 1990, MNRAS, 246, 256
Hayashi T. J., Hagiwara Y., Imanishi M., 2021, MNRAS, 504, 2675
Hayashi T. J., Hagiwara Y., Imanishi M., 2025, ApJ, 989 , 85
Heckman T. M., Smith E. P., Baum S. A., van Breugel W. J. M., Miley G. K., Illingworth G. D., Bothun G. D., Balick B., 1986, ApJ, 311, 526
Heisler C. A., Vader J. P., 1994, AJ, 107, 35
Helfand D. J., White R. L., Becker R. H., 2015, ApJ, 801, 26
Helou G., Soifer B. T., Rowan-Robinson M., 1985, ApJ, 298, L7
Imanishi M., Dudley C., Maiolino R., Maloney P. R., Nakagawa T., Risaliti G., 2007, ApJS, 171, 72
Imanishi M., Nakagawa T., Ohyama Y., Shirahata M., Wada T., Onaka T., Oi N., 2008, PASJ, 60, S489
Imanishi M., Maiolino R., Nakagawa T., 2010, ApJ, 709, 801
Intema H. T., 2014, Astrophysics Source Code Library, record ascl:1408.006
Intema H. T., Jagannathan P., Mooley K. P., Frail D. A., 2017, A&A, 598, A78
Kale R., Ishwara-Chandra C. H., 2021, Exp. Astron., 51, 95
Kellermann K. I., Condon J. J., Kimball A. E., Perley R. A., Ivezić Ž., 2016, ApJ, 831, 168
Kim D. C., Sanders D. B., 1998, ApJS, 119, 41
Kojoian G., Tovmasian K. M., Dickinson D. F., Dinger A. S. C., 1980, AJ, 85, 1462
Kuehr H., Witzel A., Pauliny-Toth I. I. K., Nauber U., 1981, A&AS, 45, 367
Kukreti P. et al., 2022, A&A, 664, A25
Lane W. M., Cotton W. D., van Velzen S., Clarke T. E., Kassim N. E., Helmboldt J. F., Lazio T. J. W., Cohen A. S., 2014, MNRAS, 440, 327
Leroy A. K. et al., 2011, ApJ, 739, L25
Lin Y.-T., Huang H.-J., Chen Y.-C., 2018, AJ, 155, 188
Lonsdale C. J., Farrah D., Smith H. E., 2006, in Mason J. W. ed., Astrophysics Update 2. Springer, Berlin, Heidelberg, p. 285
Maccagni F. M., Morganti R., Oosterloo T. A., Geréb K., Maddox N., 2017, A&A, 604, A43
Mauch T., Murphy T., Buttery H. J., Curran J., Hunstead R. W., Piestrzynski B., Robertson J. G., Sadler E. M., 2013, MNRAS, 342, 1117
McConnell D. et al., 2020, Publ. Astron. Soc. Aust., 37, e048
Morganti R., Oosterloo T. A., Capetti A., de Ruiter H. R., Fanti R., Parma P., Tadhunter C. N., Wills K. A., 2003, A&A, 399, 511
Morganti R., Oosterloo T. A., Tadhunter C. N., Vermeulen R., Pihlström Y. M., van Moorsel G., Wills K. A., 2004, A&A, 424, 119
Moshir M. et al., 1990, IRAS Faint Source Catalogue, Version 2.0, IPAC, Caltech
Murgia M., Fanti C., Fanti R., Gregorini L., Klein U., Mack K. H., Vigotti M., 1999, A&A, 345, 769
Nagar N. M., Wilson A. S., Falcke H., Veilleux S., Maiolino R., 2003, A&A, 409, 115
Nandi S., Das M., Dwarakanath K. S., 2021, MNRAS, 503, 5746
Norris R. P., Lenc E., Roy A. L., Spoon H., 2012, MNRAS, 422, 1453
O'Dea C. P., 1998, PASP, 110, 493
O'Dea C. P., Saikia D. J., 2021, A&AR, 29, 3
Offringa A. R. et al., 2014, MNRAS, 444, 606
Papadopoulos P. P., Isaak K. G., van der Werf P. P., 2010, ApJ, 720, 226
Petrov L., 2013, AJ, 146, 5
Ramos Almeida C., Tadhunter C. N., Inskip K. J., Morganti R., Holt J., Dicken D., 2011, MNRAS, 410, 1550
Rengelink R. B., Tang Y., de Bruyn A. G., Miley G. K., Bremer M. N., Roettgering H. J. A., 1997, A&AS, 124, 259
Rich J. A., Kewley L. J., Dopita M. A., 2011, ApJ, 734, 87
Rodríguez Zaurín J., Tadhunter C. N., González Delgado R. M., 2009, MNRAS, 400, 1139
Rodríguez Zaurín J. et al., 2014, A&A, 571, A57
Rovilos E., Diamond P. J., Lonsdale C. J., Lonsdale C. J., Smith H. E., 2003, MNRAS, 342, 373
Sajina A., Yan L., Lacy M., Huynh M., 2007, ApJ, 667, L17
Sanders D. B., Mirabel I. F., 1996, ARA&A, 34, 749
Sanders D. B., Soifer B. T., Elias J. H., Madore B. F., Matthews K., Neugebauer G., Scoville N. Z., 1988, ApJ, 325, 74
Schmidt M., 1963, Nature, 197, 1040
Shimwell T. W. et al., 2017, A&A, 598, A104
Sramek R. A., Tovmassian H. M., 1976, ApJ, 207, 725
Stanghellini C., O'Dea C. P., Dallacasa D., Baum S. A., Fanti R., Fanti C., 1998, A&AS, 131, 303
Stanghellini C., Dallacasa D., O'Dea C. P., Baum S. A., Fanti R., Fanti C., 2001, A&A, 377, 377
Stanghellini C., O'Dea C. P., Dallacasa D., Cassaro P., Baum S. A., Fanti R., Fanti C., 2005, A&A, 443, 891
Stern D. et al., 2012, ApJ, 753, 30
Stull M. A., 1971, AJ, 76, 1
Sulentic J. W., 1976, ApJS, 32, 171
Surace J. A., Sanders D. B., Vacca W. D., Veilleux S., Mazzarella J. M., 1998, ApJ, 492, 116
Tacconi L. J., Genzel R., Lutz D., Rigopoulou D., Baker A. J., Iserlohe C., Tecza M., 2002, ApJ, 580, 73
Tadhunter C. et al., 2018, MNRAS, 478, 1558
U V., 2022, Universe, 8, 392
Varenius E. et al., 2016, A&A, 593, A86
Veilleux S., Sanders D. B., Kim D. C., 1999, ApJ, 522, 139
Veilleux S., Kim D.-C., Sanders D. B., 2002, ApJS, 143, 315
Veilleux S. et al., 2006, ApJ, 643, 707
Veilleux S. et al., 2009, ApJS, 182, 628
Véron-Cetty M. P., Véron P., 2010, A&A, 518, A10
Waldram E., Yates J., Riley J., Warner P., 1996, MNRAS, 282, 779
Wayth R. B. et al., 2015, Publ. Astron. Soc. Aust., 32, e025
Williams P. K., Bower G. C., 2010, ApJ, 710, 1462
Wright A., Otrupcek R., 1990, PKS Catalog. Australia Telescope National Facility (ATNF), CSIRO, Sydney
Xiang L., Stanghellini C., Dallacasa D., Haiyan Z., 2002, A&A, 385, 768
Yamada S. et al., 2023, ApJS, 265, 37
Yuan T. T., Kewley L. J., Sanders D. B., 2010, ApJ, 709, 884
Yun M. S., Reddy N. A., Condon J. J., 2001, ApJ, 554, 803

APPENDIX A: INTERACTION STAGE CLASSIFICATION

Interaction class refers to the classification of galaxies based on their level of interaction or merger activity with other galaxies. According to S. Veilleux et al. (2002) there are three common phases (pre-merger, merger, and post-merger) within the interaction class on the basis of optical wavelength. Pre-merger phase is the early stages of galaxy interaction, where signs of gravitational attraction and tidal distortion due to their mutual gravitational influence can be seen. Here, the galaxies have begun to approach each other, but have not yet merged into a single entity. The detection possibility of two nuclei or dual AGN at optical, IR, and radio wavelengths is high in this phase. During the merger phase, galaxies are in the process of colliding and merging with each other. This time galaxies undergo significant morphological changes, such as the formation of tidal tails, bridges, and dis-

torted shapes. Eventually, they merge into a single, larger galaxy. Close binary nuclei or single nucleus can be detected at optical, IR, and radio wavelengths. In post-merger phase, the galaxies have already undergone a significant merger event and have coalesced into a single system. While obvious tidal features such as tails may no longer be visible, often falling below the detection threshold, many post-merger systems still exhibit disturbed central morphologies, including knots of star formation, shells, or ring-like structures. The remnant typically appears as a relaxed, high surface brightness core. Over time, the galaxy may continue to evolve through processes such as ongoing star formation and dynamical relaxation. A new AGN jet can form during this stage, which may appear as a GPS or CSS source at radio wavelengths. The Pan-STARRS optical images of each ULIRGs are shown in Figs C1 and C2, where we can see all these interaction features.

APPENDIX B: NOTES ON INTERESTING SOURCES

This appendix highlights 10 particularly interesting ULIRGs from our sample that exhibit distinctive radio morphologies, clear merger signatures, or evidence of enhanced AGN activity. These sources are discussed in more detail in this section.

IRAS 00456−2904

According to D. L. Clements et al. (1996), this galaxy's morphology suggests that it is an interacting system dominated by starburst activity, with a broad tidal tail associated with the north-east galaxy and a shorter one extending north-west from the main galaxy (see Fig. C1). The imaging analysis of S. Veilleux et al. (2006) shows that the bright south-west nucleus is a late-type galaxy, while the north-east source is of ambiguous type. These findings indicate that IRAS 00456−2904 is probably in an early-interaction phase and should be classified as a binary system (K. Dasyra et al. 2006) with a projected NS of 22.2 kpc. The *WISE* colour $W1 - W2 = 0.677$ also suggests it is a pre-merger system. The highest available 3 GHz VLASS image shows radio emission associated with the southern nucleus only (see Fig. B1). It has a small amount of extended emission towards the north-west direction at this frequency. The integrated radio spectrum shows a low-frequency turnover at 276.5 MHz and a break frequency at 2236 MHz. The maximum spectral age limit of this source is estimated to be 27 Myrs. Radio-excess fraction, spectrum, and spectral age confirm that the AGN contribution is significant for this source.

IRAS 05189−2524

The Palomar optical telescope images of the system exhibit intersecting tails and shells. D. B. Sanders et al. (1988) indicates that it is an evolved merger of two spiral galaxies (see in Fig. C1). In contrast, *Hubble* images of the system reveal off-centre nuclei, distorted outer sections, and a dim, arcing tail around the galaxies (C. A. Heisler & J. P. Vader 1994). The system is classified as a Seyfert 2 galaxy (J. A. Surace et al. 1998). Although S. Veilleux et al. (2006) classified it as a merger/interaction class, the *WISE* colour $W1 - W2 = 1.125$ indicates it is in a post/evolved merger stage. It exhibits a low turnover frequency of 361.1 MHz and a break frequency at 4317 MHz, as determined through the spectral fitting. The system is resolved at a radio frequency of 8.49 GHz, as seen in Fig. B1. The 10.9 kpc double radio structure is just at the centre of the optical host galaxy. The spectral age of the source is 1.9 Myr. The estimated q_ν value is 2.731, which shows high star formation as well. Our study indicates that IRAS 05189−2524 is hosting a buried AGN and CSS-like new young radio source.

IRAS F07599 + 6508

The galaxy has broad-line absorption and is categorized as a radio-quiet quasi-stellar object (QSO). *Hubble* images reveal clumps of emissions surrounding the QSO, which could be associated with emissions from massive stars and a recent star-forming event (L. J. Tacconi et al. 2002). *R*- and *K*-band images show the presence of tidal tails S. Veilleux et al. (2002), and the host galaxy can be seen in Fig. C1. In Fig. B1, the radio contours are overlaid on the optical image. There is no *WISE* data available for this source. The system has a low-frequency turnover at 187.6 MHz and a break frequency of 2156 MHz. The spectral age of the ULIRG is 0.21 Myr. Both GMRT images do not show any extended radio emission beyond the optical host (see Figs 2 and 3). The source is not resolved in the highest available 15 GHz data (N. M. Nagar et al. 2003). This is one of the examples which show the transformation of gas-rich mergers into radio quasars.

IRAS 11095−0238

The source IRAS 11095−0238 is the late-stage merger system with two distinct nuclei at a separation of approximately 0.5 arcsec. *Hubble Space Telescope* observations confirm that this is as a close binary system (H. A. Bushouse et al. 2002). The *WISE* colour $W1 - W2 = 1.720$ also indicates it is in a late merger stage. According to S. Veilleux et al. (2002) its interaction class is merger and the nuclear structure is single core in optical images. The Pan-STARRS image of the host galaxy (Fig. C1) exhibits features consistent with this merger scenario. The IR and radio bands show a single compact component. This object exhibits two tidal tails. The northern tidal tail is more prominent than the south-east tail (P.-A. Duc, I. Mirabel & J. Maza 1997). Optically the object is classified either as LINER (M. P. Véron-Cetty & P. Véron 2010) or as an AGN/starburst composite system (T. T. Yuan, L. J. Kewley & D. B. Sanders 2010). The spectral analysis shows a low-frequency turnover at 224.0 MHz and a high break frequency of 3.0×10^{13}MHz. To obtain the maximum spectral age, the highest frequency available for flux measurements is taken as the break frequency. The maximum spectral age of this system is <19 Myr. The highest frequency radio data available for this galaxy is the 3 GHz VLASS image and the source is unresolved at this frequency. The low-frequency turn over can be due to two merging radio active nuclei, but it needs high resolution radio observations to detect the components.

IRAS 12265 + 0219

This source is very bright and is a famous radio-loud quasar commonly known as 3C273 at a redshift of $z = 0.158$ (M. Schmidt 1963). The estimated q_ν value of this source is -1.300 and it is also the most luminous radio source in our sample (log $L_{1.4\mathrm{GHz}}$ = 27.699 WHz^{-1}). This object is highly nucleated but shows a thick tidal feature toward the north-east and a very faint feature to the north-west (S. Veilleux et al. 2002). Its host galaxy is an elliptical one (see in Fig. C2), and it shows all the characteristics that are typical of high-luminosity quasars including a flat radio spectrum of the core, rapid and strong variability in all observed

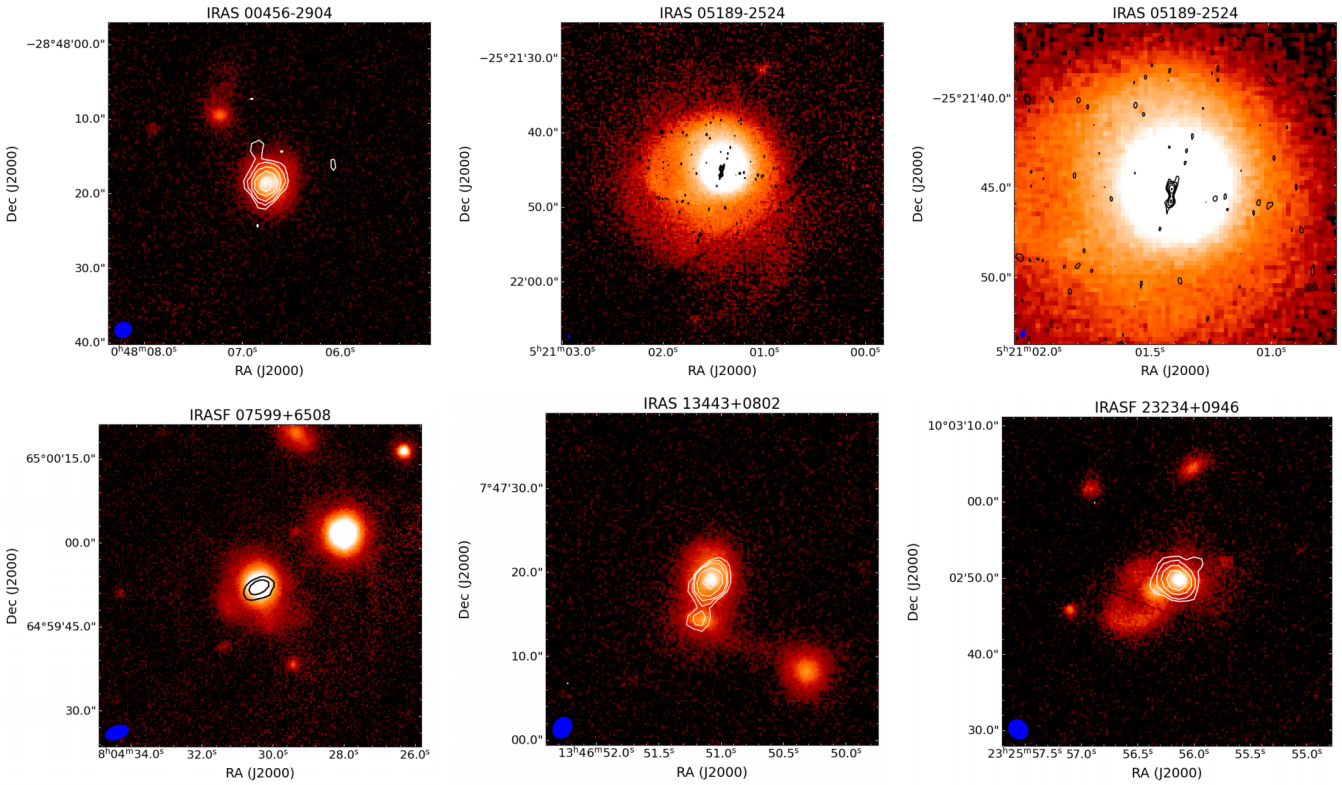

Figure B1. Contours from the highest available radio-frequency maps overlaid on Pan-STARRS optical images of the five ULIRGs. Radio contours start at 3σ and increase by factors of 2, where σ represents the local rms noise level: 3.594×10^{-4}, 1.5×10^{-4}, 9.759×10^{-4}, 3.0×10^{-4}, and 3.639×10^{-4} Jy beam^{-1} for IRAS 00456−2904, IRAS 05189−2524, IRAS F07599+6508, IRAS 13443+0802, and IRAS F23234+0946, respectively.

energy ranges, variable polarization, and a radio jet with superluminal motion (U. Bach et al. 2007). According to *WISE* colour and S. Veilleux et al. (2002) it is a merger system. The spectral analysis shows a high break frequency of 5.9773×10^6 MHz but no turnover frequency. To obtain the maximum spectral age, the highest frequency available for flux measurements is taken as the break frequency. The spectral age of this system is <0.0093 Myr. The highest frequency data which we have used for this galaxy is the 22 GHz VLA image. This image does not show any resolved morphology. This source show a transformation the gas-rich merger remnant into a radio-loud quasar.

IRAS 13428 + 5608

This source is known as Mrk 273, and exhibits a striking tidal tail towards the south (see in Fig. C2). This is a rare example of very extended radio emission. LOFAR detected 300 kpc radio emission for this object (P. Kukreti et al. 2022).This is a late-stage merger with three nuclei at the centre. Though S. Veilleux et al. (2002) noted merger interaction class but *WISE* colour represents its a evolved merger phase. Initially the north and south-west nuclear components were detected through IR observations, while the south-east component is detected through radio observations. Later high-resolution observations indicate detection of north nucleus in radio also (C. L. Carilli & G. B. Taylor 2000). The positions of these three AGNs are shown in J. Rodríguez Zaurín et al. (2014). The radio AGNs are not on the brightest region of the optical host galaxy. For radio spectrum fitting, we used central core flux density but not the northern or southern arc. The GMRT detected extended emission in both bands, as seen in Figs 2 and 3. The spectral fitting gives a low-frequency turnover at 115.7 MHz, a break frequency at 4891 MHz. The estimated spectral age is 3.5 Myrs\. Although our study did not resolve the central part of the source, optical images indicate that the source is young with multiple nuclei.

IRAS 13443 + 0802

IRAS 13443 + 0802 is clearly involved in interactions with two other objects (see in Fig. C2). All three sources within this field are classified as emission-line galaxies with an H II region-type spectrum, sharing similar redshifts ($z = 0.135$). This triple system comprising a close pair with an NS of ∼5 arcsec (∼12 kpc) in the north–south direction, along with a third galaxy located ∼15 arcsec (∼35 kpc) to the south-west of that pair (C. Tadhunter et al. 2018). According to the paper by S. Veilleux et al. (2002), there is a possibility that a bridge of material may be present between the eastern binary and the south-west component. Two detected *WISE* components show one AGN and one star-forming region is interacting in this system. This system has a break frequency at 1997 MHz but no turnover frequency. The spectral age is estimated to be 0.43 Myr, indicating this source is a relatively young radio source. Fig. B1 shows the 3 GHz radio contours overlaid on the optical image. It clearly resolved two nuclei and indicates that the north is brighter than the south nucleus. Radio peak positions are separated by 7.552 arcsec. The presence of binary AGNs is possible for this system but it needs to be confirmed by performing high-resolution multifrequency observations.

IRAS 13451 + 1232

Another name of this target is PKS 1345 + 12. It is identified as a quasar and stands out as one of the nearest bright GPS/CSS radio sources. This quasar has been considered a prime candidate for acting as a link between ULIRGs and young radio galaxies (R. Morganti et al. 2004). It is the second most luminous radio source in our sample ($\log L_{1.4\mathrm{GHz}} = 26.305$ WHz^{-1}) and the estimated q_ν value is −0.361. The host galaxy of this source is undergoing a pre-merger process. This is indicated by the presence of a double nucleus, irregular isophotes, a tail, and the existence of several nearby smaller companions these features strongly suggest that the merging process has triggered the observed radio activity (T. M. Heckman et al. 1986). The optical image reveals two distinct nuclei, separated by approximately 2 arcsec (4 kpc), as shown in Fig. C2 (L. Xiang et al. 2002). The primary concentration of activity occurs within the western nucleus, identified as a Sy2 in the optical spectrum (S. Veilleux, D. B. Sanders & D. C. Kim 1999) and as a compact source in radio wavelengths (A. S. Evans et al. 1999). The VLBI observations revealed the inner structure into twin lobes and a core (C. Stanghellini et al. 2001) with a projected linear size < 150 pc. In our analysis, the integrated radio spectrum has a low-frequency turnover at 359.1 MHz. The break frequency of this target is at 7666 MHz which gives a spectral age estimate of 0.21 Myr. Double nuclear components have been detected in optical, IR, and radio.

IRAS* 15327 + *2340

This is a well-known interacting system, Arp 220. The morphology of Arp 220, showing a double nucleus structure in optical, radio, and IR. The optical host galaxy is shown in Fig. C2. Its tidal tails and dust lanes, indicate that it is likely the outcome of a recent merging phenomenon. E. Varenius et al. (2016) reported steep spectrum outflows and extended emission at 150 MHz. The estimated q_ν value is 2.593 which is above the mean value of 2.34 (M. S. Yun et al. 2001), indicates that most of its radio emission comes from strong starburst activity. According to E. Rovilos et al. (2003), this galaxy exhibits very powerful maser emission and does not belong to the category of compact symmetric objects or medium symmetric objects. This source exhibits low frequency turnover at 291.2 MHz and the break frequency is 7.0789×10^5 MHz. To obtain the spectral age for this source we take the highest frequency available for flux measurements as a lower limit of the break frequency. Therefore, the lower limit of spectral age is estimated to be < 0.76 Myr.

IRAS F23234 + 0946

This is a double nucleus system in both optical and IR. A hooklike tidal tail is present and it extends to the south-east as seen in Fig. C2. The two nuclei are situated in the east and west, with the western nucleus showing no sign of AGN activity in the MIR spectrum and displaying the highest brightness at optical wavelengths M. Imanishi et al. (2007). According to J. Rodríguez Zaurín (2009), the western nucleus has a much higher percentage contribution of old stellar population (60–82 per cent) compared to the eastern nucleus when these two are compared. The estimated q_ν value for this source is 2.250. To obtain the spectral age for this source we use the highest frequency available for flux measurements is taken as the break frequency. This source exhibits no turnover frequency. The break frequency is 1.6343×10^4 MHz. The 3 GHz VLASS archival image provides the highest frequency radio data for this source. The radio synchrotron age is estimated to be < 0.14 Myr. The western nucleus shows distinct radio emission (Fig. B1). Hence, we expect AGN activity in the western component also.

APPENDIX C: PAN-STARRS OPTICAL IMAGES OF ULIRGS IN OUR SAMPLE

This appendix shows the Pan-STARRS optical images of the ULIRGs studied in this work. These images are included to complement the discussion in Section 4.4, where we describe the optical appearance of the host galaxies. The Pan-STARRS images provide a view of the host galaxy morphologies and help illustrate features such as disturbed structures, tidal signatures, and possible multiple components, which are relevant for understanding the interaction and merger status of these systems.

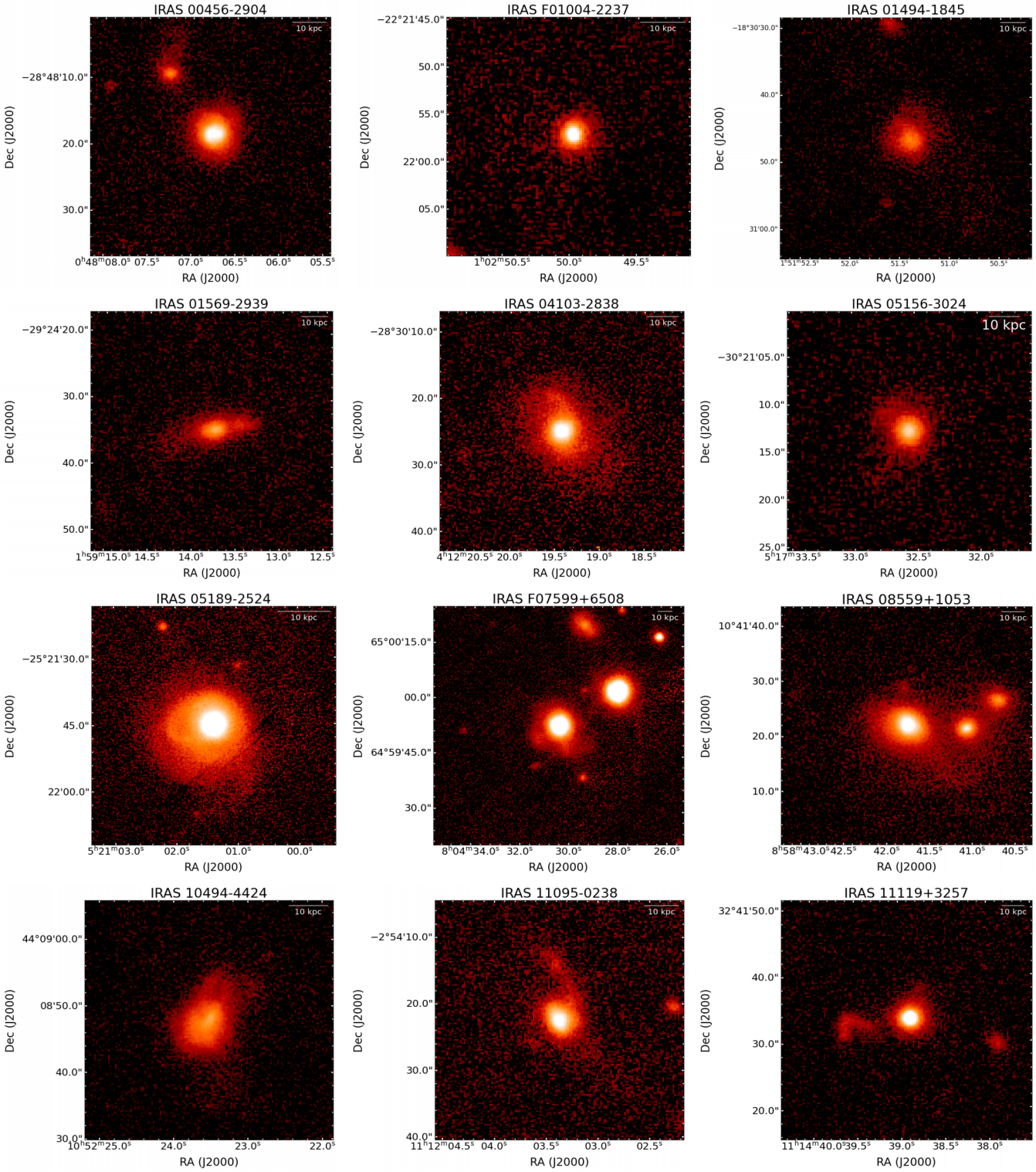

Figure C1. Pan-STARRS images of host galaxy of source IRAS 00456−2904, IRAS F01004−2237, IRAS 01494−1845, IRAS 01569−2939, IRAS 04103−2838, IRAS 05156−3024, IRAS 05189−2524, IRAS F07599+6508, IRAS 08559+1053, IRAS 10494 + 4424, IRAS 11095−0238, and IRAS 11119 + 3257.

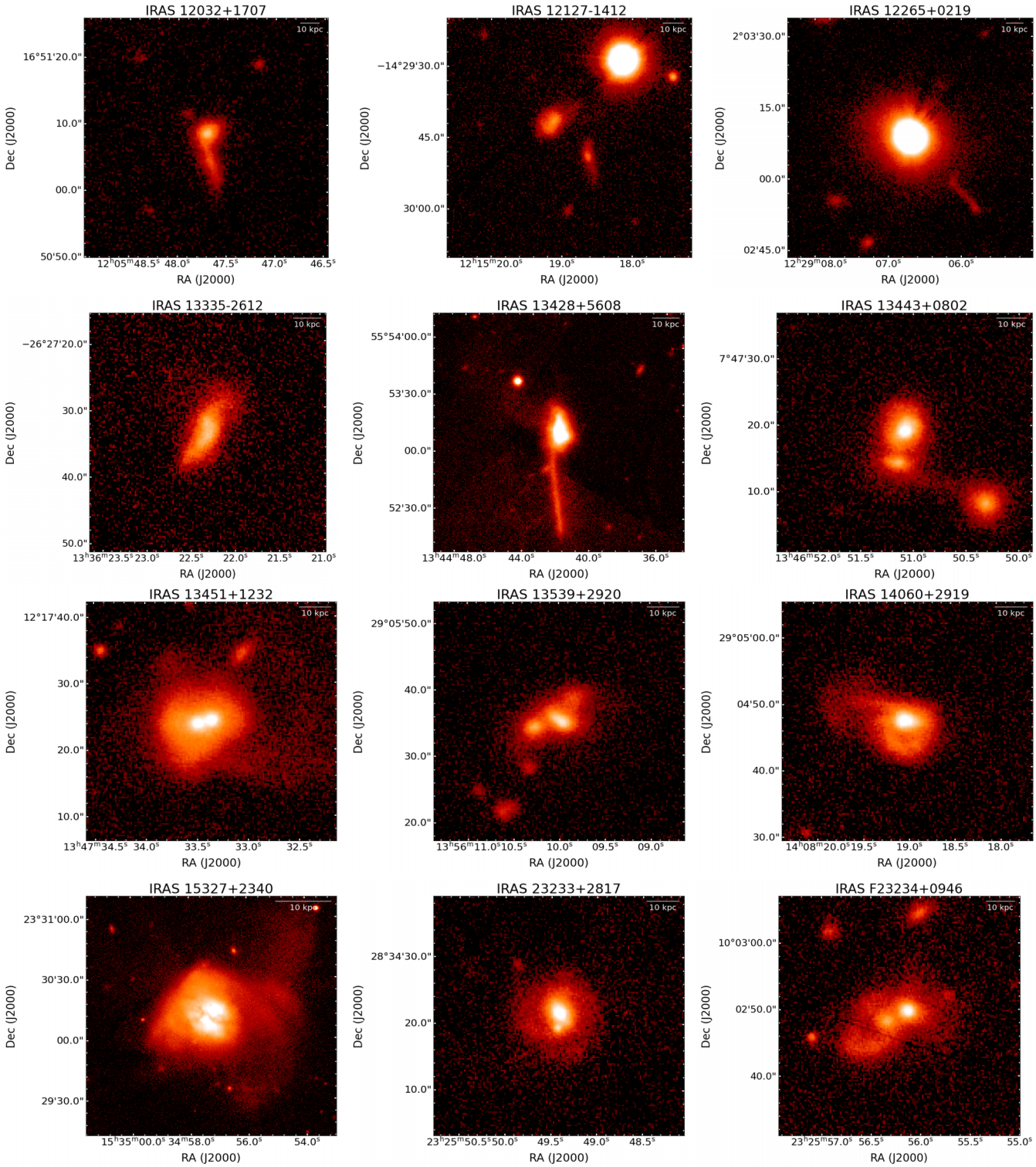

Figure C2. Pan-STARRS images of host galaxy of source IRAS 12032 + 1707, IRAS 12127−1412, IRAS 12265 + 0219, IRAS 13335−2612, IRAS 13428+5608, IRAS 13443+0802, IRAS 13451+1232, IRAS 13539+2920, IRAS 14060+2919, IRAS 15327+2340, IRAS 23233+2817, and IRAS F23234 + 0946.

This paper has been typeset from a TEX/LATEX file prepared by the author.